Aerodynamically induced formation of contrails

K. Gierens*, B. Kärcher, H. Mannstein, B. Mayer
DLR Oberpfaffenhofen, Institut für Physik der Atmosphäre, Germany

Keywords: Aerodynamics, Microphysics, Optics, Contrails

ABSTRACT: We study the formation and growth of ice particles induced by the cooling of the air while flowing over the wings of cruising aircraft.

1 INTRODUCTION

Photographs taken in flight show that condensation sometimes starts right above the wings of cruising aircraft. This demonstrates the existence of contrails different from the well studied jet exhaust contrails. Below we present a first investigation of the conditions that lead to the appearance of aerodynamic contrails, along with a characterisation of their basic microphysical and optical properties. Studies of aerodynamic contrails require interdisciplinary research on compressible gas flow over airfoils, ice and aerosol microphysics, and optics of ice crystals, such as outlined here.

2 AERODYNAMICS

As a first step into this new research area, we make simplifying yet sufficiently accurate assumptions that allow us to compute the flow field by straightforward numerical means, circumventing the use of a sophisticated CFD code. As a motivation, we start with a simple back-of-the-envelope calculation.

2.1 *Back-of-the-envelope calculation*

The average pressure difference above minus below the wings is the force that carries the aircraft. Let the aircraft weight be W, its wing area A, then the pressure difference is $\Delta p = -W/A$. For wide body aircraft (e.g. A340, B747) this amounts to a surprisingly large value of typically −50 hPa. Now assume that this pressure difference arises adiabatically in the flow. The corresponding temperature difference is given by $\Delta T / T = [(\kappa-1)/\kappa] (\Delta p / p)$ with $\kappa = c_p/c_V = 1.4$ being the ratio of the specific heats of air. For typical conditions at cruise altitudes (e.g. T = 220 K, p = 220 hPa) we get $\Delta T = -14$ K, i.e. a sudden cooling above the wing that suffices to turn even relatively dry air of, say, $RH_i = 20\%$, into a transient supersaturated state that may allow condensation. This rough calculation suggests that aerodynamically induced condensation should occur at times. The question arises why, on the contrary, it apparently is a rare event. In order to answer this and other questions, we have to perform a more detailed flow calculation.

2.2 *Linearised 2-dimensional flow calculation for compressible flow*

We assume that the flow is adiabatic and circulation free, furthermore that the flow is strictly two-dimensional and stationary. First we define the shape of the airfoil, i.e. the cross section of the wing. We have chosen a simple analytical shape, the Joukowski wing. This already quite realistic wing shape results from a conformal mapping of a unit circle, which is appropriate for our goal (although the Joukowski wing is not used in practice). In particular, it has one sharp (trailing) and one round (leading) edge. If we had an incompressible flow, we could compute the velocity potential and stream functions for the Joukowski wing simply from the corresponding quantities in a flow around a circular cylinder. The analytical form of the latter is known, and applying the same con-

* *Corresponding author:* Klaus Gierens, DLR-Institut für Physik der Atmosphäre, Oberpfaffenhofen, D-82234 Wessling, Germany. Email: Klaus.Gierens@dlr.de

formal mapping to these fields as to the wing shape (i.e. the Joukowski transformation) yields the desired result. However, flow incompressibility requires flow speeds with small Mach numbers, while modern airliners typically cruise at Ma = 0.8. Therefore, we must not assume that the flow is incompressible, and we need another way of computation.

The details of our method will be given elsewhere, here we only present the essential assumptions that lead to the solution. Under the stipulated assumptions, the continuity and Euler equations combine to an equation for the flow potential Φ. We assume that the parallel background flow, (u_∞, v_∞), is perturbed only little by the wing and that the background flow has a small angle of attack relative to the wing. With these assumptions, we may linearise the potential equation. Then perturbations caused by the thickness of the wing and by its camber can be treated separately and are additive, leading to the following ansatz for the potential:

$$\Phi = u_\infty x + v_\infty y + \varphi + \psi, \tag{1}$$

where φ and ψ are the perturbation potentials for wing thickness and camber, respectively. Neglecting perturbation quantities of quadratic and higher order in the equation for the potential then gives:

$$\beta^2 \varphi_{xx} + \varphi_{yy} = 0 \quad \text{and} \quad \beta^2 \psi_{xx} + \psi_{yy} = 0 \text{ with } \beta^2 = 1 - Ma^2 \tag{2}$$

The simple (non-conformal) coordinate transformation $x = \xi$, $\beta y = \eta$, yields the classical Laplace equation for the potentials, for instance $\varphi_{\xi\xi} + \varphi_{\eta\eta} = 0$, which can be solved by various means. We employ the method of singularities, where the perturbation potentials are constructed by suitable superpositions of potentials for singular sources, sinks, and vortices.

From the flow field, we computed a set of trajectories, both below and above the wing, using a 4th-order Runge-Kutta scheme (Press et al., 1989). The perturbation of the (dominating) x-component of the flow speed on the trajectories, $u - u_\infty$, is inserted into a generalised Bernoulli equation to yield the temperatures along the trajectories, viz.

$$T = T_\infty - [(\kappa - 1)/\kappa \, R_a] \, (u^2 - u_\infty^2)/2 \tag{3}$$

where R_a is the specific gas constant of dry air (287 J kg^{-1}K^{-1}). The corresponding pressure is obtained from the Poisson equation, viz.

$$p = p_\infty \, (T / T_\infty)^{\kappa/(\kappa-1)}. \tag{4}$$

Figures 1 and 2a/b show the flow field (streamlines) and the temperature and pressure histories on the trajectories for a case with p_∞ = 350 hPa and T_∞ = 235 K. The wing depth is 11.7 m, wing thickness 1.7 m, and the effective angle of attack is 1°.

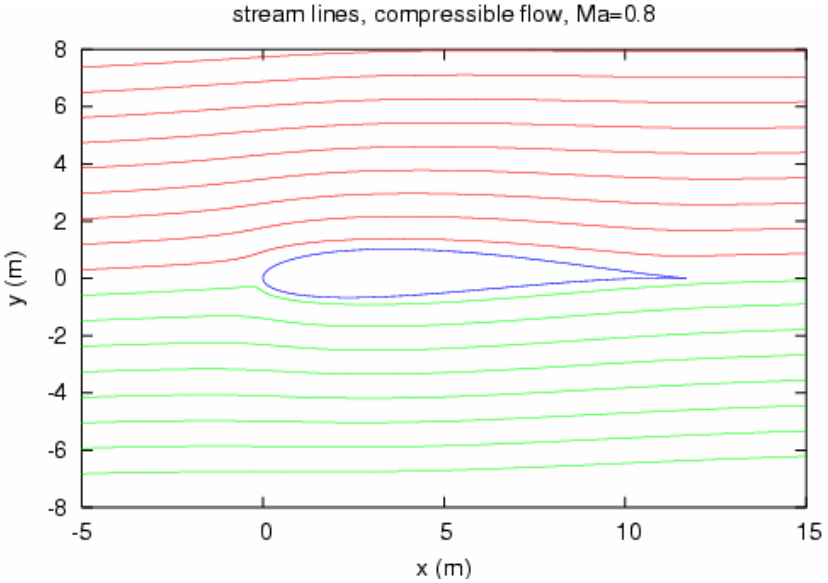

Figure 1. Two-dimensional potential flow field (compressible flow) around a Joukowski airfoil, calculated with the method of singularities. Effective angle of attack: 1°. Mach number: 0.8. The dimensions of the airfoil are typical of a wide-body aircraft close to the fuselage.

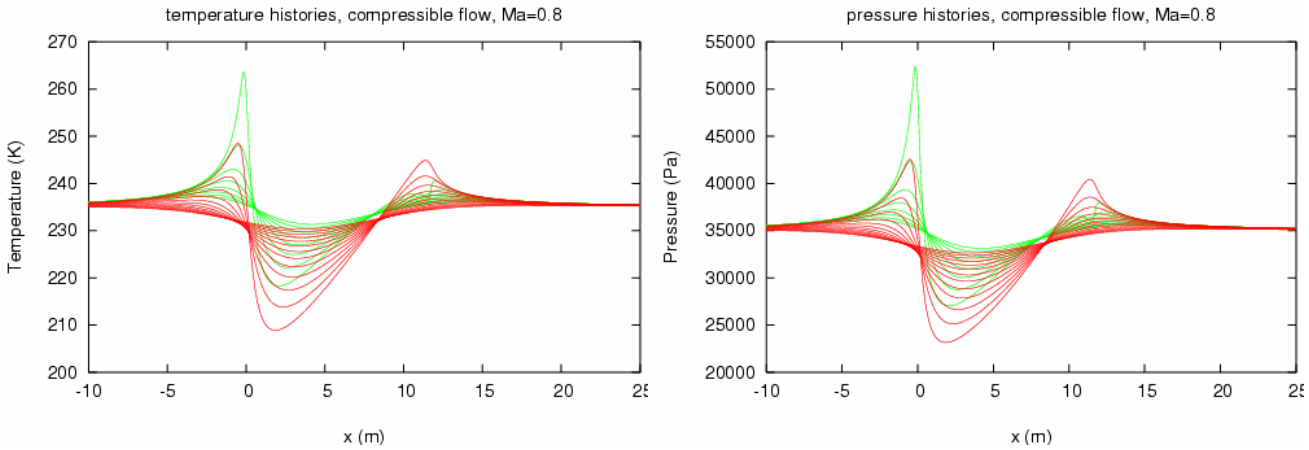

Figure 2. Temperature (left) and pressure (right panel) histories along the streamlines shown in Figure 1.

3 MICROPHYSICS

We employ a comprehensive gas-aerosol-ice trajectory model (Kärcher, 2003) to track the following non-equilibrium processes along one of the T- and p-trajectories close to the wing as shown above. (i) Water condensation on liquid aerosol droplets composed of aqueous H_2SO_4. (ii) Homogeneous freezing of ice from these supercooled aerosol particles. (iii) Depositional growth of the spherical ice particles.

Water uptake on particles is coupled with the gas phase in a strictly mass-conserving manner, so that the evolution of the supersaturation is accurately simulated. A relatively broad lognormal aerosol size distribution has been used for aerosols (mean mass radius 80 nm, geometric standard deviation 1.6, total number concentration 500 cm^{-3}) to cover both Aitken and accumulation mode sizes. Growth of aerosol particles is treated in a Lagrangian manner. This allows us to accurately simulate the water mass fraction in each particle size category to which freezing nucleation rates are extremely sensitive. Growth of ice particles is treated with a moving centre size structure that is virtually free of numerical diffusion. We prescribe an ambient ice supersaturation of RH_i = 140% just below the homogeneous freezing threshold and an H_2O deposition coefficient of unity to maximize ice particle growth. We use a time step of 1 µs for these simulations.

Figure 3 shows results of the microphysical calculations. The legend denotes times and corresponding distances behind the leading wing edge. The ice crystal size distributions (solid curves) are generated from homogeneous freezing of liquid aerosol droplets (dashed). Nucleation is finished as the air parcel moves across the wing (after ~16 m). In the subsequent growth phase in the highly supersaturated air, mean ice particle radii increase to ~2.8 µm after ~680 m.

Note that the ice particle spectrum becomes essentially monodisperse shortly after nucleation. Laminar flow and monodispersity are the key prerequisites for the colourful appearance of aerodynamic contrails, as studied in Section 4. Jet exhaust contrails, on the contrary, appear white because plume turbulence quickly mixes contrail ice particles with slightly different sizes and thus broadens their size spectrum.

Interestingly, the smallest droplets freeze first, followed by freezing of larger droplets, until practically all available aerosol particles are depleted. At first glance, this seems to contradict the common notion that larger particles freeze first owing to their larger volume. However, this assumes that aerosol particles are in equilibrium with ambient H_2O, regardless of size. During the formation of aerodynamic contrails, RH_i changes dramatically on the time scale of ~10 µs. This is of the same order as the composition change time scale dictated by diffusion of H_2O molecules in air. For the small aerosol particles, the latter time scale is proportional to particle surface area. This implies that they adjust faster to increasing RH_i and become water-rich much faster than larger particles, and hence freeze earlier despite a smaller volume. The fact that the time scale for a change in radius is somewhat longer than the time scale for freezing explains why the ice particles start to grow significantly only after nucleation is shut off. It is possible that more and slightly smaller ice

particles would form if we prescribed a larger concentration of aerosol particles. These and other aspects will be addressed in more detail in future work by means of sensitivity studies.

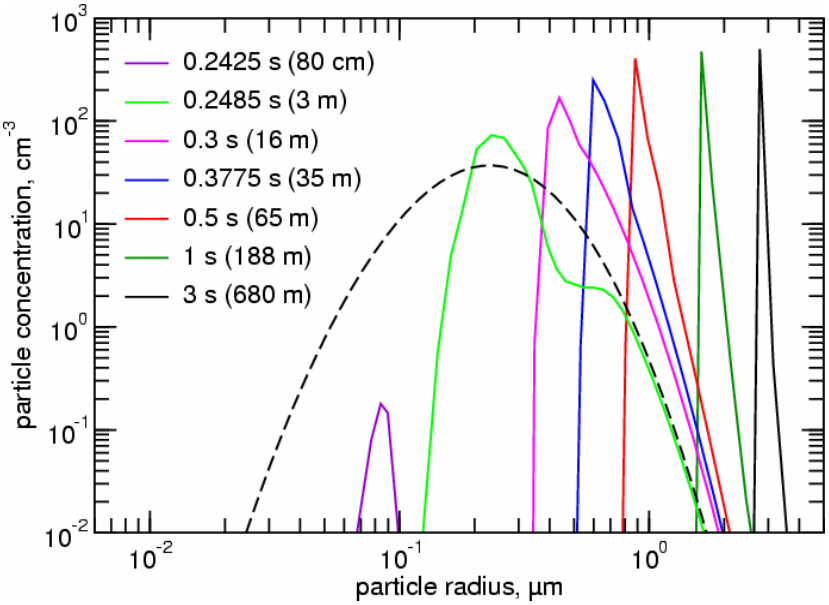

Figure 3. Ice crystal size distributions for various distances (times) behind the leading edge of the wing along the trajectory closest to and above the wing.

4 RADIATION

To determine the colour of the contrail, the scattering coefficient was calculated from the size distributions in Figure 3 using the theory by Mie [1908] for spherical ice particles. The well-known Mie code by Wiscombe [1979] as provided by the libRadtran radiative transfer package [Mayer and Kylling, 2005] was used for this purpose.

Figure 4a shows the extinction efficiency at 550 nm (solid line) as function of the particle radius. The typical features of a monodisperse particle distribution are clearly visible: the Rayleigh limit for particles much smaller than the wavelength, where the extinction efficiency increases rapidly with particle size; and the geometrical optics limit for particles much larger than the wavelength, where the extinction efficiency approaches 2 (that is, the extinction cross section is twice the geometrical cross section). In the size range where the particle radius is comparable to the wavelength, the extinction efficiency shows characteristic oscillations and reaches its maximum where the radius equals the wavelength of the radiation. In the visible spectral range, absorption is negligible and the scattering efficiency equals the extinction efficiency.

From these considerations we may immediately conclude that the scattering coefficient of a monodisperse particle distribution strongly depends on wavelength; if illuminated with white light, selective scattering of colours will cause the scattered radiation to be coloured: e.g., crystals with 400 nm radius will scatter blue most efficiently and the scattered radiation will appear blue; crystals with 700 nm will appear red as the maximum of the scattering cross section occurs at 700 nm. For a polydisperse size distribution, these effects are reduced, and if the size distribution is too wide, they will vanish completely. Hence the appearance of colours indicates a narrow size distribution.

To calculate the actual colour of the contrail, a full radiative transfer calculation is required in principle, to calculate spectral radiance. However, since the optical thickness is small we used a very simple single-scattering approximation: the scattered radiance is assumed to be proportional to the incident (extra-terrestrial) irradiance times the scattering coefficient. This calculated spectral irradiance is converted to colours using “specrend” by John Walker, available at http://www.fourmilab.ch/documents/specrend/. Spectral radiance is converted to X, Y, and Z using the respective CIE colour matching functions, which are then converted to device-dependent colour-coordinates R, G, and B with the respective EBU matrix.

Figure 4a shows the calculated colours as a function of ice particle radius for a monodisperse size distribution. As outlined above, colours are most pronounced in the size range where the change of the extinction efficiency with wavelength is strongest. Figure 4b, finally, shows the colours to be expected for the size distributions from Figure 3. Size distributions were provided every 0.001 seconds from 0.24 seconds to 6 seconds. Extinction efficiencies were calculated with Mie theory and integrated over the size distribution to get the spectral extinction coefficient, multiplied with the spectral extraterrestrial irradiance, and converted to colours. Figure 4b shows the effective ice particle radius. The colours nicely match the colours in the photograph, indicating that growth with time as well as the width of the size distribution were realistic.

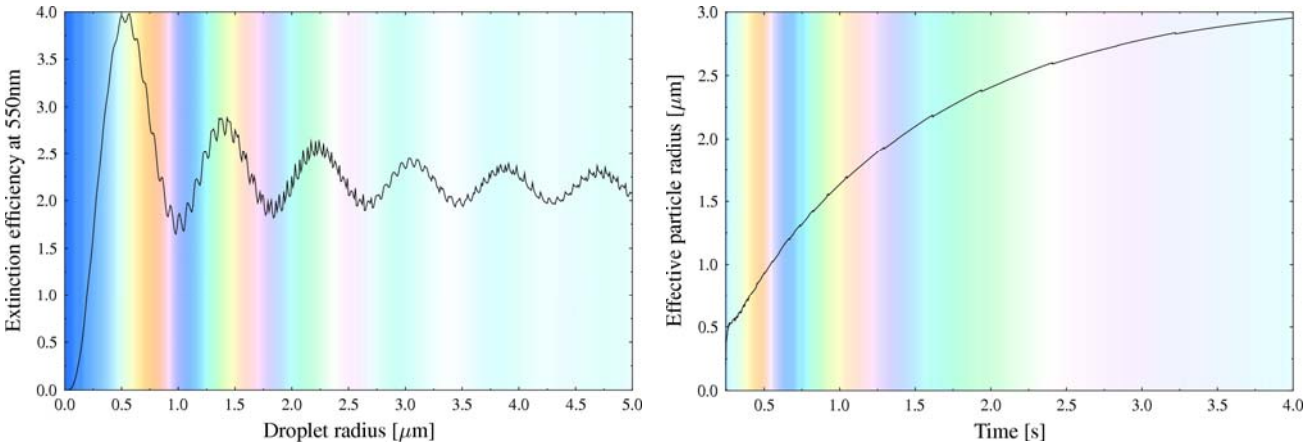

Figure 4. (a) Extinction efficiency for a monodisperse ice particle distribution and colour of the scattered radiation in single-scattering approximation; (b) effective radius and colour for the size distributions from Figure 3 as a function of time.

5 EXAMPLE

On 12 June 2005 from 14:59 to 15:06 Bejing time (~07:00 UTC), pilot and photographer Jeff Well took a series of photos of an exceptionally colourful iridescent contrail produced by an A340-313X aircraft in 9600 m altitude, just 1200 m above his position on the same route over eastern China. Both aircraft were heading to North-West (329°) from 32° 14.8' N, 119° 46.7' E to 32° 56.8' N, 119° 10.1' E. From NCEP reanalysis data we estimate a temperature of –40°C, the aircraft altitude is very close to the 300 hPa pressure level.

The series of photos displayed in Figure 5 shows the development of contrails that cannot be explained by the Schmidt-Appleman criterion. Jet contrails produced from the mixing of exhaust gases with the ambient air would show up as 4 separate lines behind the engines and start later. The onset of the aerodynamic contrails occurs directly above the wings and is stronger close to the body of the aircraft. Thin vortex lines originate from the wing tips and get mixed into the wake vortices.

6 CONCLUSIONS AND OUTLOOK

Photographs demonstrate that aerodynamic contrails occur preferentially above the inner parts of the wings, where the uplift is largest. Hence, aerodynamic contrails may become more relevant for a potential future fleet of blended wing-body aircraft with significantly larger wing depths.

Future work will study the properties of the numerous small ice crystals produced in the adiabatic air flow over wings of airliners, the impact of ambient conditions and background aerosol properties on early aerodynamic contrail formation and evolution, and how common this process occurs relative to jet exhaust contrails that form according to the Schmidt-Appleman theory.

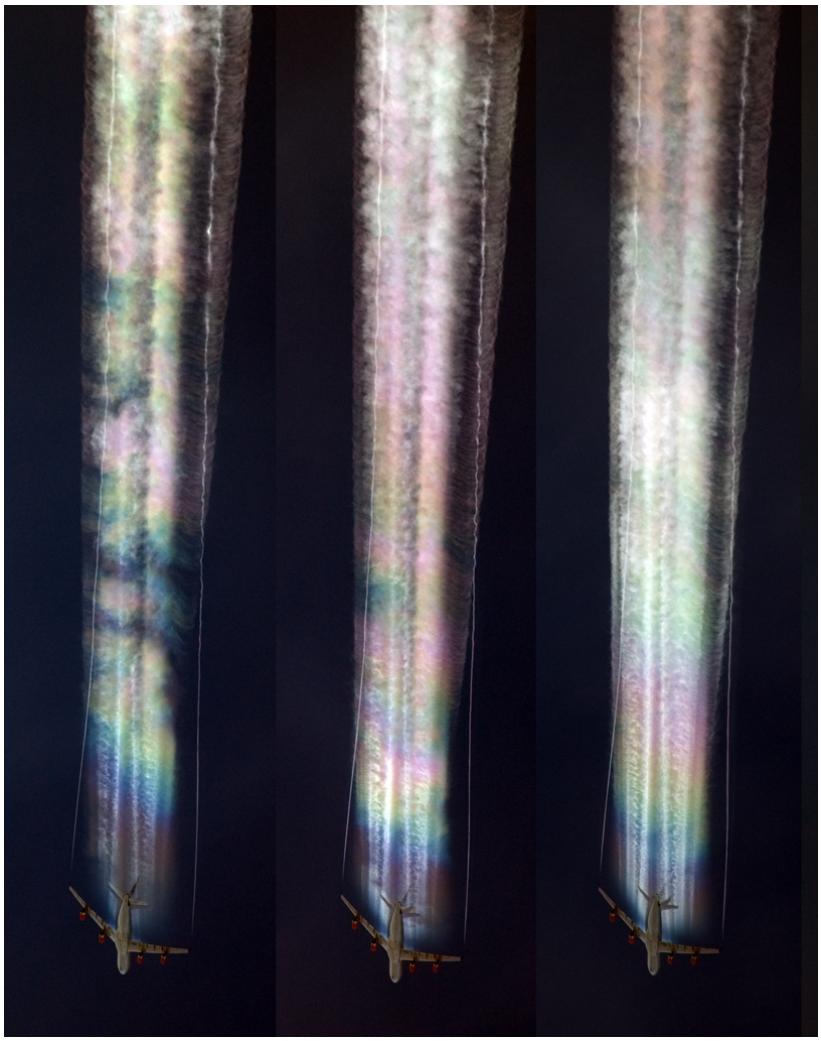

Figure 5. Series of photographs of an aerodynamically induced contrail. Note the iridescent colours. The formation and colourful appearance of such contrails are explained by the combination of aerodynamical, microphysical, and radiative processes outlined in this paper.

ACKNOWLEDGEMENT

The photographs shown here are all taken by pilot Jeff Well. We thank Jeff Well for allowing us to use his photographs of aerodynamic contrails. Many other photographs of aerodynamic contrails can be found on www.airliners.net. This work is supported by the DLR/HGF project Particles and Cirrus Clouds (PAZI-2).

REFERENCES

Kärcher, B., 2003: Simulating gas-aerosol-cirrus interactions: Process-oriented microphysical model and applications. *Atmos. Chem. Phys, 3,* 1645–1664.

Mayer, B., and A. Kylling, 2005: Technical Note: The libRadtran software package for radiative transfer calculations: Description and examples of use. *Atmos. Chem. Phys., 5,*1855–1877.

Mie, G., 1908: Beitraege zur Optik trueber Medien, speziell kolloidaler Metalloesungen. *Annalen der Physik*, Vierte Folge, 25(3):377–445.

Press, W.H., B.P. Flannery, S.A. Teukolsky, and W.T. Vetterling, 1989: *Numerical Recipes.* Cambridge University Press, Cambridge, UK, ISBN 0 521 38330, 702 pp.

Wiscombe, W.J., 1996: Mie Scattering Calculations: Advances in Technique and Fast, Vector-Speed Computer Codes. Technical Report TN-140+STR, NCAR, 1979, edited and revised 1996.

Contrails in a global climate model – effect of reducing systematic errors

A. Guldberg*
Danish Meteorological Institute, Copenhagen, Denmark

Keywords: Contrails, radiative forcing, systematic errors

ABSTRACT: The contrail parameterization of Ponater et al. (2002) has been implemented in the global climate model IFSHAM. The global mean net radiative forcing due to contrails is in this model positive, but small, and in areas over Europe and the United States the net forcing is negative. In order to investigate this result a series of experiments has been performed modifying contrail optical properties. Results from these experiments are shown. The climate model exhibits certain systematic errors and the impact of these systematic errors is analysed. The model is run in nudged mode, where the model is relaxed towards observed data thereby reducing the systematic errors of the model substantially. Comparing runs with the model in standard mode and in nudged mode gives the possibility for analysing the impact of model systematic errors on contrail properties and contrail radiative forcing. Results from these experiments are shown as well.

1 INTRODUCTION

The radiative forcing due to line shaped contrails was given a best estimate of 20 mW/m^2 in the IPCC special report "Aviation and the Global Atmosphere" (IPCC, 1999) for 1992 air traffic conditions. There is some uncertainty on this estimate and some of the results published later indicate smaller values for the contrail radiative forcing.

Marquart et al. (2003) has implemented the contrail parameterization scheme of Ponater et al. (2002) in the global climate model ECHAM4 and simulations with this model give an estimate of the radiative forcing due to line shaped contrails of 3.5 mW/m^2 – an order of magnitude smaller than the IPCC estimate. The same contrail parameterization as used in Marquart et al. (2003) has been implemented in the global climate model IFSHAM (Guldberg and Nielsen, 2004). Using this model setup simulations similar to the Marquart et al. (2003) simulations result in an estimate of radiative forcing due linear contrails of 0.26 mW/m^2 – an order of magnitude smaller than the Marquart et al. (2003) estimate. The geographical distribution of the radiative forcing shows areas – over Europe and the United States – where the net radiative forcing is negative. This is not seen in the results of Marquart et al. (2003) – here the net forcing is positive everywhere.

In order to be able to explain the reason for this very small and in some areas negative radiative forcing in the simulations of the IFSHAM model two sets of experiments were performed. In one set contrail optical properties were modified in order to study the impact of these properties. In another set of experiments the impact of model systematic errors were investigated. The IFSHAM model has as all global models systematic errors and in the experiments performed here these systematic errors were substantially reduced using the nudging technique, where the model is forced to follow observed data. Comparing with simulations in standard climate mode the importance of the systematic errors for the estimation of contrail radiative forcing was studied.

2 MODEL AND EXPERIMENTS

The IFSHAM model is developed at DMI (Yang, 2004) as a combination of the dynamical core from ARPEGE, version 3 (Déqué et al. 1994) and the physical parameterization package from

* *Corresponding author:* Annette Guldberg, Danish Meteorological Institute, Lyngbyvej 100, 2100 Copenhagen, Denmark. Email: ag@dmi.dk

ECHAM5 (Roeckner et al. 2003). The IFSHAM model uses semi-Lagrangian advection and a two-level semi-implicit time stepping scheme. The cloud scheme is the PCI scheme (Lohmann and Roeckner, 1996), where cloud water and cloud ice are treated as separate prognostic variables. The radiation scheme consists of the Morcrette short wave scheme (Morcrette, 1991) and the RRTM scheme (Mlawer et al., 1997) for the long wave part. Contrails are described by the parameterization scheme of Ponater et al., 2002. The resolution of the model used in these experiments is T63 with 31 vertical layers.

2.1 *Optical properties*

In order to investigate the impact of contrail optical properties on contrail radiative forcing a set of one year long experiments were performed in which the optical properties effective radius and optical depth were modified. The effect of changing the effective radius on the radiative forcing was minor in these experiments – for results see Guldberg and Nielsen (2004).

The optical depth of contrails is parameterized in IFSHAM and is a function of ice water path and ice water content. A set of sensitivity experiments were performed in which the optical depth was fixed at a constant value. Figure 1a shows the resulting annual mean contrail net radiative forcing at the top of the atmosphere (TOA) from a one year long experiment with a variable optical depth determined by the parameterization scheme whereas figure 1b shows the net radiative forcing also from a one year long experiment, but with the optical depth set to a constant value of 0.1. The global mean of the contrail coverage is relatively low in these experiments: 0.07 %.

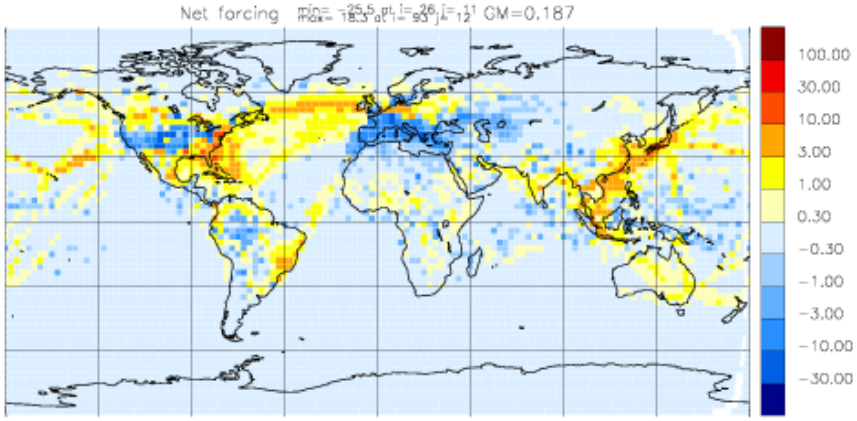

Figure 1a Annual mean of net radiative forcing at TOA from an experiment with variable optical depth (Unit: mW/m^2)

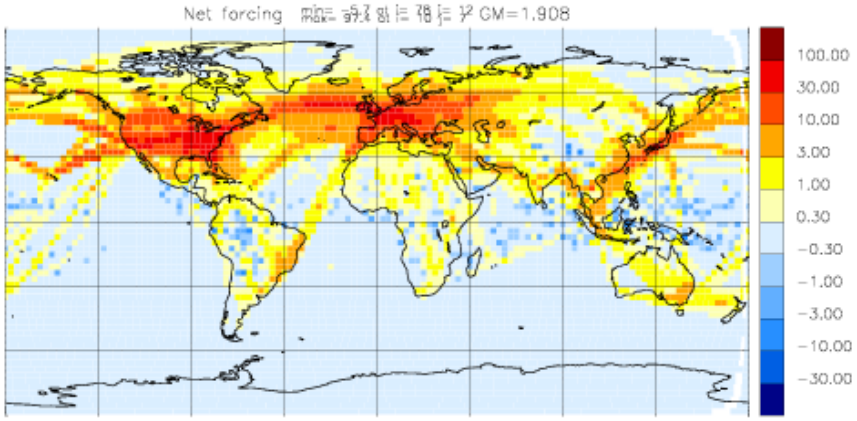

Figure 1b Annual mean of net radiative forcing at TOA from an experiment with constant optical depth of 0.1 (Unit: mW/m^2)

Fixing the optical depth at a constant value of 0.1 leads to a substantial increase in the short wave forcing but an even larger increase in the long wave forcing and therefore the resulting net forcing is also substantially increased. The global mean of the net forcing is 0.2 mW/m^2 in the experiment with variable optical depth and 1.9 mW/m^2 in the experiment with an optical depth of 0.1. This means a factor of ten larger net forcing in the experiment with constant optical depth. It is also seen

when comparing figure 1a and 1b that the areas over Europe and the United States with negative net forcing in the experiment with variable optical depth have a positive net forcing in the experiment with constant optical depth. From these experiments it is seen that optical depth has a large impact on the estimation of contrail radiative forcing.

2.2 *Systematic errors*

As all climate models the IFSHAM model suffers from certain long term systematic errors when compared to observations and these errors may influence the estimation of contrail properties. In order to analyse the effect of model systematic errors simulations were performed with the model in so called nudged mode. Using the nudging technique (Jeuken et al., 1996) the model is forced towards a reference data set, and when the reference data set represents observed data the systematic errors of the model are minimized, because in each time step the model is following closely the observed values of the prognostic variables. Nudging is a simple 4-dimensional assimilation of the reference data, where the prognostic model variables are relaxed towards the reference data. In the experiments described here the ECMWF Re-Analysis data (ERA-15) (Gibson et al., 1997) are used as the reference data set towards which the model is relaxed.

Two sets of simulations have been performed with the IFSHAM model in order to study the impact of systematic errors. In the first set – the standard simulations – the model is forced with observed sea surface temperatures for ten winter seasons and ten summer seasons in the period covered by the ERA-15 data set (1973-1993). In the second set – the nudged simulations – the model is run in nudged mode and the model is relaxed towards observed data for the same ten winter and summer seasons and also observed sea surface temperatures are used. In the following only averages of the ten summer seasons are shown. Results for the winter season can be found in Guldberg and Nielsen, 2004.

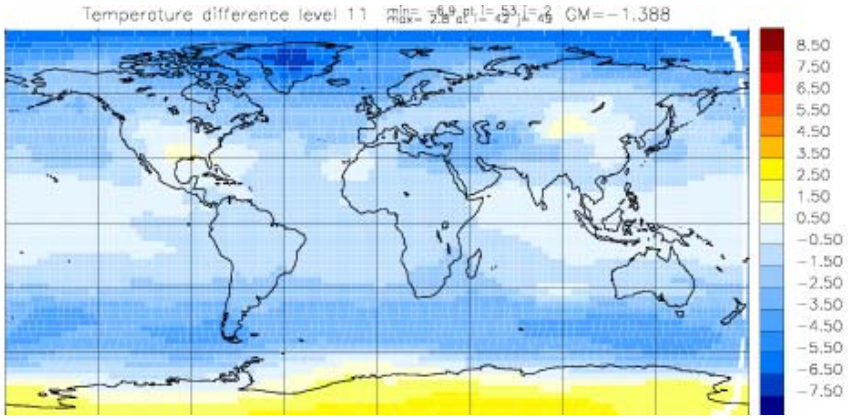

Figure 2a Ten year mean difference of temperature between standard and nudged simulations at ~240 hPa (Unit: K)

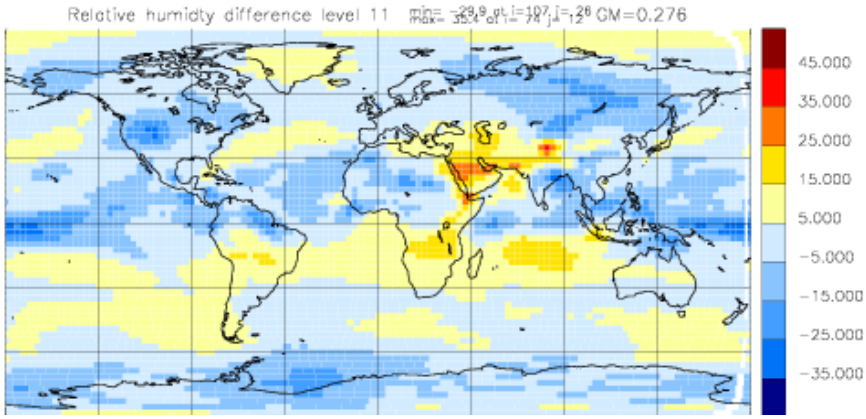

Figure 2b Ten year mean difference of relative humidity with respect to ice between standard and nudged simulations at ~240 hPa (Unit: %)

Figure 2a shows the average difference of temperature between the standard and the nudged simulations at approximately 240 hPa. This difference represents well the temperature systematic error of

the model as the nudged simulation follows closely the ERA-15 data. It is seen that in summer the model is too cold almost everywhere, except over Antarctica where the model is too warm. The largest cold biases are seen at northern high latitudes.

Figure 2b is similar to figure 2a but shows relative humidity with respect to ice. In summer the relative humidity with respect to ice is too low in most of the Northern hemisphere. It should be noted that humidity is not nudged in these experiments, so the humidity in the nudged simulations are determined by the model based on close to observed values of the other prognostic variables.

The annual global mean of the contrail coverage in these simulations is 0.13 % and the model systematic errors have little impact on the contrail coverage. But the differences actually seen between the two model simulations follow to a large degree the pattern of the differences of the relative humidity, indicating that relative humidity is likely the determining factor for these differences. Also differences in ice water path between the standard and the nudged simulations are rather small, but there is a tendency of too large values in the tropics and too small values in the extratropics in the standard simulations. As the effective radius and the optical depth are determined from the ice water path, the same tendency is seen for the effective radius and the optical depth. More detailed information on these differences can be found in Guldberg and Nielsen (2004).

The main question is how the model biases affect the radiative forcing of contrails in the IFSHAM model. Figure 3a and 3b show the changes in the short wave and long wave forcing. As the sign of the short wave forcing is negative positive values in the difference plot in figure 3a mean that the magnitude is too low in the standard simulation. For the summer season the magnitude of the short wave forcing is too low over the northern part of the United States, the North Atlantic flight corridor and northern Europe. In the southern part of the United States and southern Europe the magnitude of the forcing is too large in the standard simulation. The global mean of the short wave forcing is increased by 0.4 mW/m^2 when the model is nudged. The long wave forcing is too weak, respectively too strong in the areas where the short wave forcing is too weak, respectively too strong. The global mean of the long wave forcing is increased by 0.6 mW/m^2, when the model is nudged.

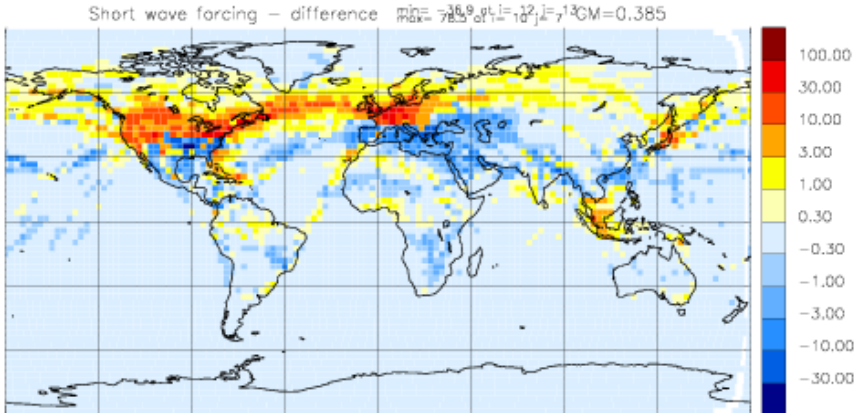

Figure 3a Ten year mean difference of short wave radiative forcing at TOA between standard and nudged simulations (Unit: mW/m^2)

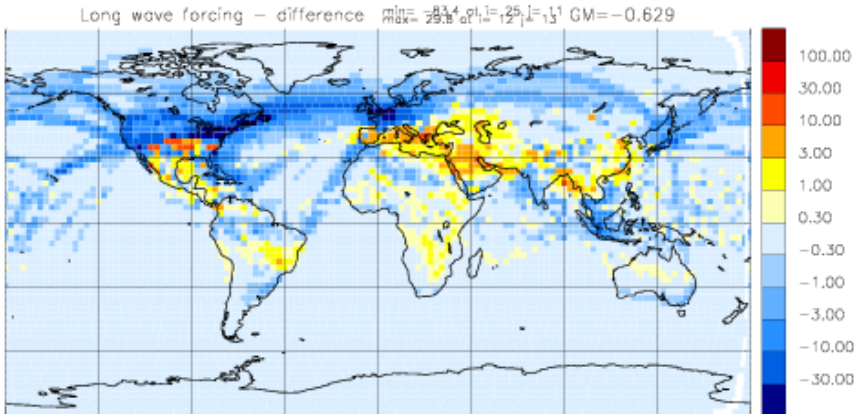

Figure 3b Ten year mean difference of long wave radiative forcing at TOA between standard and nudged simulations (Unit: mW/m^2)

Figure 4a and 4b show the contrail net radiative forcing at TOA in the standard simulation and the nudged simulation of the summer season. The global mean of the net forcing is increased by 0.2 mW/m^2 from 0.8 mW/m^2 to 1.0 mW/m^2. Although the magnitude of the net forcing is changed the pattern of the forcing is to a large degree unchanged.

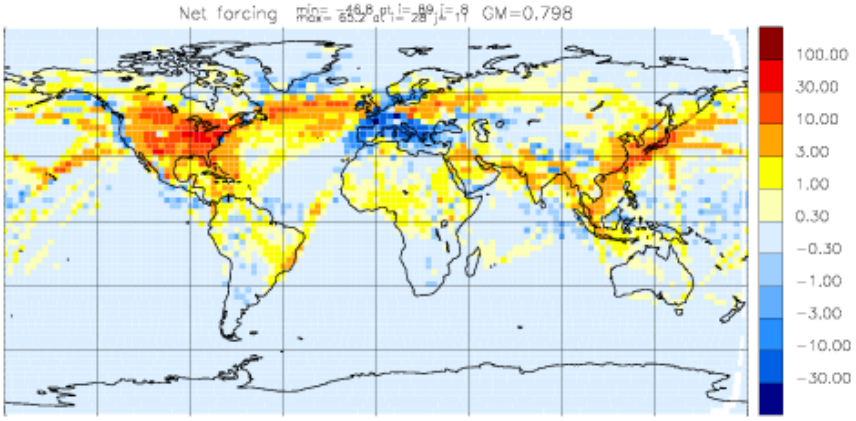

Figure 4a Ten year mean of net radiative forcing at TOA for standard simulation (Unit: mW/m^2)

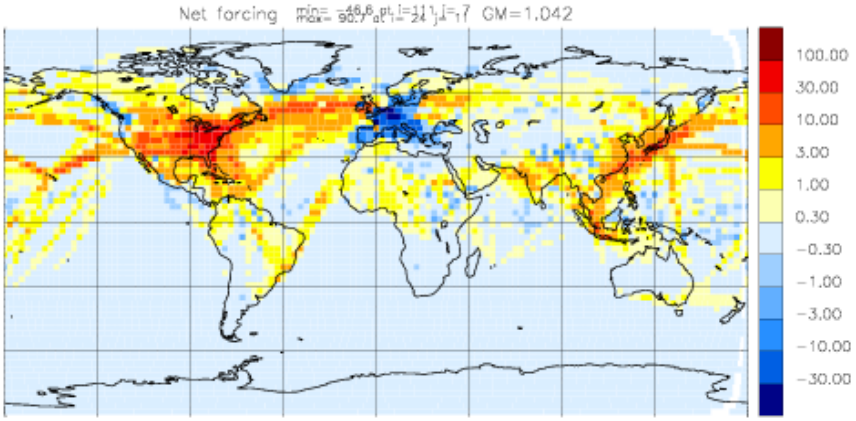

Figure 4b Ten year mean of net radiative forcing at TOA for nudged simulation (Unit: mW/m^2)

3 CONCLUSIONS

The contrail parameterization of Ponater et al. (2002) has been implemented in the IFSHAM model. The net radiative forcing due to contrails is in this model an order of magnitude smaller than obtained by Marquart et al. 2003. Furthermore the net forcing shows areas with negative values.

In order to investigate the reasons for these results experiments with modifications of the optical properties of the contrails have been performed. It turns out that setting the optical depth to a constant value of 0.1 results in a net radiative forcing in better agreement with other results. Furthermore the areas over Europe and the United States with negative net forcing do in the experiment with constant optical depth have positive net radiative forcing. But the question is how realistic it is to set a constant value for the optical depth.

The impact of systematic errors of the model have been studied using the nudging technique. The systematic errors are causing a 10-20 % too low estimate of the short and long wave forcing. The net forcing is 75 % too low in winter and 20 % too low in summer in the standard mode compared to the nudged version of the model. But the geographical distribution of the net forcing is unchanged and areas with negative net forcing still exist.

In order to understand better the model estimation of contrail radiative forcing a detailed investigation of the radiation parameterization for both short and long wave radiation is needed. Also an analysis of the many different parameterizations of optical properties available could be of importance for understanding the effect of contrails on the radiation balance.

REFERENCES

Déqué, M. C. Dreveton, A. Braun and D. Cariolle, 1994: The ARPEGE/IFS atmosphere model: a contribution to the French community climate modelling. *Climate Dynamics,* 10:249-266.

Gibson, J. K., P. Kållberg, S. Uppala, A. Hernandez, A. Nomura and E. Serrano, 1997: *ERA-15 Description,* Volume 1 of ECMWF Re-analysis Project Report Series, ECMWF, Reading, UK.

Guldberg, A. and J. K. Nielsen, 2004: *Contrails and their climate impact,* Scientific Report 04-06, DMI, Denmark, www.dmi.dk/dmi.sr04-06

IPCC, 1999: *Aviation and the global atmosphere,* Cambridge University Press, Cambridge, UK.

Jeuken, A. B. M., P. C. Siegmund, L. C. Heijboer, J. Feichter and L. Bengtsson, 1996: On the potential of assimilating meteorological analyses in a global climate model for the purpose of model validation, *J. Geophys. Res.,* 101:16939-16950.

Lohmann, U. and E. Roeckner, 1996: Design and performance of a new cloud microphysics scheme developed for ECHAM general circulation model. *Climate Dynamics,*12:557-572.

Marquart, S., M. Ponater, F. Mager and R. Sausen, 2003: Future Development of Contrail Cover, Optical Depth and Radiative Forcing: Impacts of Increasing Air Traffic and Climate Change. *Journal of Climate Change,* 16:2890-2904.

Mlawer, E. J., S. J. Taubman, P. D. Brown, M. J. Ianoco and S. A. Clough, 1997: Radiative transfer for inhomogenous atmospheres: RRTM, a validated correlated-k model for the longwave. *Journal of Geophysical Research,* 102:16663-16682.

Morcrette, J.-J., 1991: Radiation and cloud radiative properties in the European Centre for Medium Range Weather Forecasts forecasting system, *J. Geophys. Res.,* 96:9121-9132.

Ponater, M., S. Marquart and R. Sausen, 2002: Contrails in a comprehensive global climate model: Parameterization and radiative forcing results. *Journal of Geophysical Research (Atmosphere),* 107(D13):ACL 2 1-15.

Roeckner, E., G. Bäuml, L. Bonaventura, M., R. Brokoph, M. Esch, M. Giorgetta, S. Hagemann, I. Kirchner, L. Kornblueh, E. Manzini, A. Rhodin, U. Schlese, U. Schulzweida and A. Tompkins, 2003: *The atmospheric general circulation model ECHAM5. Part I: Model Description,* Max-Planck-Inst. Meteorol. Rep., 349, Germany.

Yang, S., 2004: The DKCM Atmospheric Model. The Atmospheric Component of the Danish Climate Model, Danish Climate Centre Report 04-05, DMI, Denmark

Comparison of cirrus cloud coverage calculated from reanalysis meteorological data with satellite data

L. Lim*, D.S. Lee
Dalton Research Institute, Department of Environmental & Geographical Sciences, Manchester Metropolitan University, UK

R. Ismail, R.G. Grainger
Sub-Department of Atmospheric, Oceanic and Planetary Physics, University of Oxford, UK

K. Gierens, M. Ponater
Institut für Physik der Atmosphäre, Deutsches Zentrum für Luft and Raumfahrt (DLR), Oberpfaffenhofen, Germany

Keywords: Cirrus cloud, satellite, reanalysis meteorology

ABSTRACT: An offline cirrus cloud coverage calculation was conducted using a parameterisation similar to that adopted in ECHAM (Chen et al., 1997), as part of a preliminary analysis from ongoing work on estimating the uncertainties from contrail radiative forcing. The resulting cirrus cloud coverage, calculated from ECMWF ERA-40 reanalysis specific humidity and temperature data, was compared with ISCCP cirrus cloud data. Monthly mean results showed that computed coverage statistics between 45° South and 45° North were comparable with those from satellite observations. Similar spatial coverage structures, i.e. the high and low coverage values, were captured by both the parameterised calculation and the ISCCP dataset. A sensitivity analysis on the critical value of relative humidity over ice (U_{ci}) necessary for clouds to form highlights the importance of selecting an appropriate value of U_{ci}, optimized for the meteorological dataset used.

1 INTRODUCTION

The IPCC 'Aviation and the Global Atmosphere' report (1999) identified contrails and cirrus clouds as being, potentially, the largest effects from aviation on radiative forcing. This work forms part of a wider investigation to identify the sources of uncertainties in estimating radiative forcing from contrails. Cirrus coverage is required to determine which fraction of a grid cell is available for potential contrail formation. Therefore, it is important to compare calculated cirrus cloud coverage with observations.

2 METHODOLOGY

2.1 *Cirrus cloud parameterisation*

A method to calculate contrail coverage has previously been published by Sausen et al., 1998. The first stage of this work uses this method to produce an offline model that calculates the cirrus cloud coverage from different sources of meteorological data. In order to produce a suitable coverage map, it is necessary to have access to sufficiently resolved meteorological data in time and space. The European Centre for Medium-Range Weather Forecasts (ECMWF) Re-Analysis (ERA-40) datasets fulfil these criteria. From these datasets, fractional cirrus cloud coverage is calculated from specific humidity and temperature data using a parameterisation similar to that adopted for the general circulation model, ECHAM (Chen et al., 1997).

* *Corresponding author:* Ling Lim, Dalton Research Institute-CATE, Manchester Metropolitan University, Faculty of Science and Engineering, John Dalton East Building, Chester St, Manchester M1 5GD, UK. Email: l.lim@mmu.ac.uk

Fractional cirrus cloud coverage (cirrus cloud by levels), b_{ci}, is calculated from Equation (1), where U_i is the relative humidity over ice and U_{ci} the critical value of relative humidity over ice. Total cirrus cloud coverage (over different levels) was then calculated from b_{ci} using random and maximum overlap assumptions (Sausen et al., 1998).

$$b_{ci} = 1 - \sqrt{\frac{1 - \max(U_i, U_{ci})}{1 - U_{ci}}} \tag{1}$$

The parameter U_{ci} determines whether cirrus cloud will form in a particular grid box, i.e. U_{ci} has to be exceeded for cirrus cloud to form (Sundqvist, 1978). Generally, U_{ci} is optimized for a given General Circulation Model (GCM) in order to yield a cloud distribution that leads to an optimal closure of the global annual radiation balance at the top of the atmosphere. If a modification is made to the resolution of a GCM or the cloud-radiative interaction, then the radiation balance at the top of the atmosphere may be disturbed. It is therefore necessary to restore the radiative balance either by modifying parameters affecting the cloud optical properties or by modifying the U_{ci} value. Various U_{ci} values have been used for previous ECHAM runs, e.g. ECHAM3 (U_{ci} = 0.85), ECHAM4 (U_{ci} = 0.6), ECHAM4.L39 (U_{ci} = 0.7).

In this preliminary work, total cirrus cloud calculated using U_{ci} = 0.6 (as adopted by Sausen et al., 1998) is compared with satellite data. U_{ci} values ranging from 0.5 to 0.85 are then applied to the parameterisation to determine the sensitivity of U_{ci} in predicting cirrus cloud coverage using ERA-40 data.

2.2 *Satellite data*

The International Satellite Cloud Climatology Project (ISCCP) was established in 1982 to produce global, reduced resolution datasets of basic properties of the atmosphere from which cloud parameters could be derived (Rossow et al., 1996). Five geostationary and two polar orbiting satellites have been used to infer the global distribution of cloud properties and their diurnal, seasonal and inter-annual variations. ISCCP analysis correlates radiances measured by satellites with temperature, humidity, ice and snow from TOVS (TIROS Operational Vertical Sounder) in order to determine information about clouds and the surface. Satellites (apart from TOVS) which cover January 1999 are NOAA-12, NOAA-14, GOES-8, METEOSAT-5 and GMS-5.

2.3 *Comparison study*

In this work we select a way of evaluating cirrus coverage that is directed towards identifying the sources of uncertainties in the intended contrail coverage analysis. Factors taken into consideration include the availability of satellite data, temporal resolution and high air traffic movement regions (Europe, North America, North Atlantic corridor and the Far East). Table 1 provides a summary of the data used to produce cirrus cloud coverages for this initial comparison work.

Table 1: Data used in the comparison study (U_{ci} = 0.6)

	Meteorology	Satellite
Dataset	ECMWF ERA-40	ISCCP climatological summary product (D2)
Parameters	Specific humidity and temperature	Daytime cloud (cirrus) amount (%)
Year	January 1999	January 1999
Horizontal resolution	2.5° x 2.5° globally	Equal area grid, latitudinally 2.5°
Vertical range	500 to 50 hPa	440 to 50 hPa
Temporal resolution	Monthly mean calculated from 00, 06, 12, 18 UTC	Monthly mean calculated from 00, 03, 06, 09, 12, 15, 18 and 21 UTC

3 RESULTS AND DISCUSSION

3.1 *Comparison between cloud parameterisation and observations*

The resulting cirrus cloud coverage for the case where U_{ci} = 0.6 (Figure 1) is compared with observed global cloud data from the ISCCP dataset (Figure 2) for one calendar month (January 1999).

In this study, only data for latitudes between 45° South and 45° North were used to evaluate cirrus coverage from the cirrus parameterisation and ISCCP.
This initial attempt indicates that a longer time period, such as one year or more, is necessary because there are not enough data from ISCCP at important contrail-affected regions such as North America and Northern Europe (mainly due to January being a winter month). A comparison of the calculated cirrus cloud coverages with the ISCCP dataset shows that ISCCP has a higher maximum coverage (99%) and mean value (30%) than the calculated maximum coverage (92%) and mean value (24%) from the ERA-40 dataset.

Relative maxima of cirrus coverage were calculated over Polynesia in the Pacific Ocean, Amazon basin, central Africa and along the Inter Tropical Convergence Zone (ITCZ). These are similar to the ISCCP data, even though the ISCCP cirrus coverage in these areas was higher than that calculated from ERA-40 data. Relative minima were calculated over the East Pacific Rise, Central America, North Africa and India. Similar structures were observed in ISCCP data but again with higher values. Spatial patterns from both sources were comparable but computed coverages lacked the finer details that were observed in ISCCP data.

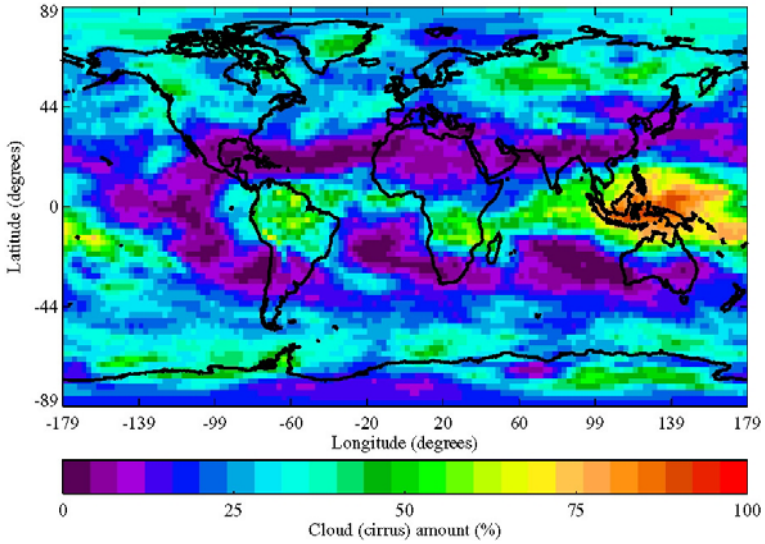

Figure 1. Cirrus cloud coverage calculated from ERA-40 data using ECHAM parameterisation for reference case ($U_{ci} = 0.6$)

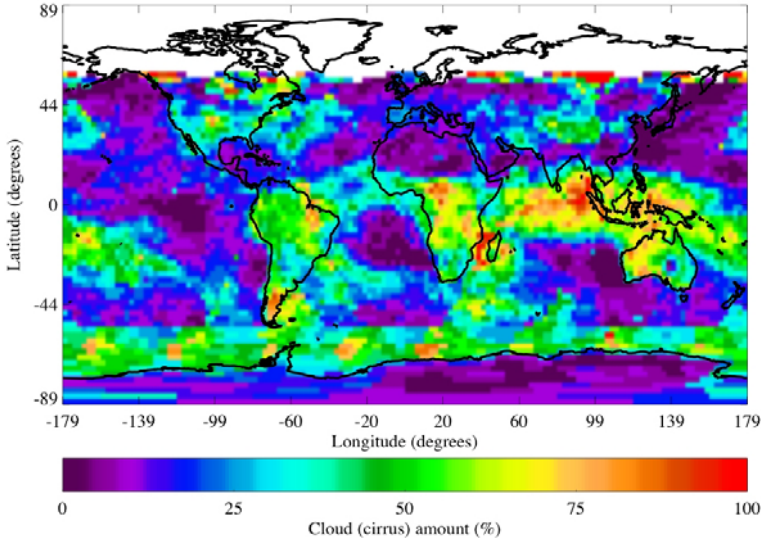

Figure 2. Cirrus cloud coverage from ISCCP

3.2 *Sensitivity of U_{ci}*

Results of the sensitivity analysis on U_{ci} in predicting cirrus cloud coverage using ERA-40 data are presented in Table 2. As expected, there is a variation of global mean coverage values for different U_{ci} values. The lowest U_{ci} value tested (0.5) produced the highest maximum coverage (92.9%) and the highest global mean coverage (30.3%). There was a gradual decrease of maximum and global

mean coverage with increasing U_{ci}. For U_{ci} = 0.5 and U_{ci} = 0.85, there was a difference of 6% for the maximum coverage and 14% for the global mean coverage. In this preliminary study, even though the global mean coverage decreases approximately linearly with increasing U_{ci}, this is not reflected on a cell-by-cell basis.

Table 2: Comparison of global coverage statistics

Statistic	Parameterisation (%)							
U_{ci}	0.5	0.55	0.6	0.65	0.7	0.75	0.8	0.85
Maximum	92.9	92.5	92.1	91.5	90.8	89.9	88.8	87.2
Mean	30.3	28.5	26.6	24.7	22.8	20.9	18.9	16.8

Spatial plots for U_{ci} = 0.5 and U_{ci} = 0.85 are presented in Figures 3 and 4, respectively. These show that they have the same basic patterns but the structural details are different. For instance, low cirrus cloud coverage (< 12%) was observed in both figures over the Pacific Ocean, west of Mexico. However, the low coverages from the U_{ci} = 0.85 test case extend further northwards onto the west coast of the United States when compared with the coverage produced using U_{ci} = 0.5.

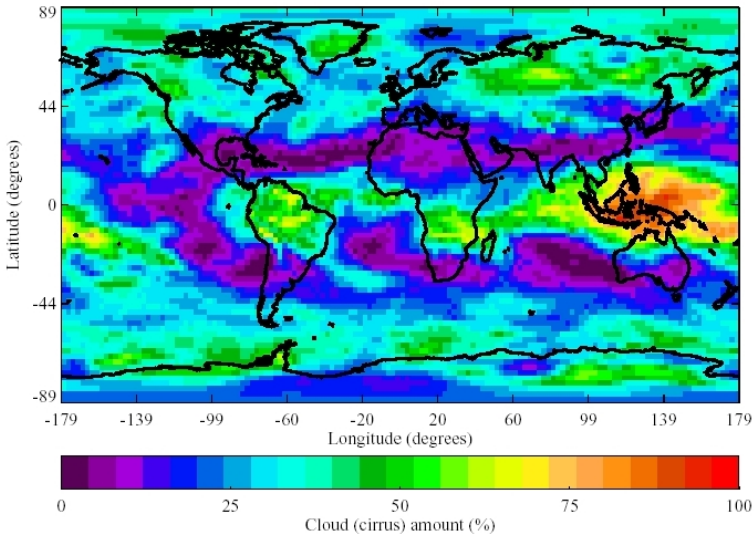

Figure 3. Cirrus cloud coverage calculated from ERA-40 data using ECHAM parameterisation for test case U_{ci} = 0.5

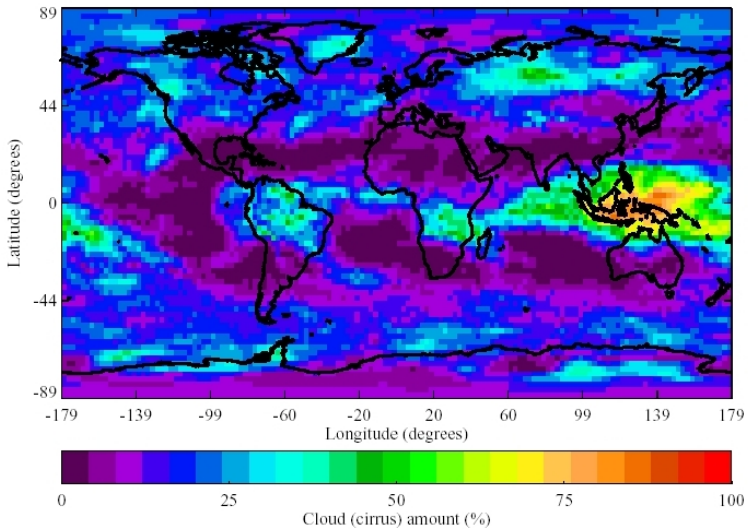

Figure 4. Cirrus cloud coverage calculated from ERA-40 data using ECHAM parameterisation for test case U_{ci} = 0.85

The results of this sensitivity analysis demonstrate the importance of selecting an appropriate U_{ci} value for the meteorological dataset used. This value may influence the spatial distribution of cirrus coverage calculations and, therefore, the global mean coverage. A possible approach is to optimize the U_{ci} value to the high cloud field inherent in the ERA-40 dataset. Theoretically, the U_{ci} values

can be below 0.5 (the lower limit tested) and higher than 0.85 (the upper limit tested) (Walcek, 1994). Therefore, it is possible to further adjust U_{ci} for ERA-40 data to produce an optimized cloud distribution for regions with high aircraft movements.

4 CONCLUSIONS AND FURTHER WORK

Cirrus cloud coverage is an important parameter in estimating the uncertainties for contrail coverage as it is required to determine which fraction of a grid cell is available for potential contrail formation. There was good agreement between the cirrus cloud coverage calculated using the ECHAM cirrus cloud parameterisation and the dataset obtained from ISCCP. Spatial patterns from both sources were comparable with each other. However, computed coverages lacked the finer details that were observed in ISCCP data.

January 1999 ISCCP data did not have enough data capture (due to January being a winter month) for important contrail coverage regions such as high air traffic regions in North America and Northern Europe. Hence, a longer time period is necessary to yield an evaluation that serves the purpose of this study. There are also other data sources for cirrus climatology that can be used for such a comparison, such as SAGE and HIRS data (well established) and the University of Oxford's MIPAS and GRAPE datasets (under development). However, ISCCP is still the most widely used and commonly accepted dataset.

A sensitivity analysis on U_{ci} showed the importance of this parameter in determining cirrus coverages resulting from the parameterisation. The first step in the next stage of work is to optimize U_{ci} for the ERA-40 dataset to match its global high cloud dataset. Then, U_{ci} can be optimized for latitudes with high air traffic and then tested in other regions. Other planned further work includes comparison of calculated coverage using this new U_{ci} value; comparisons of different temporal statistics (diurnal, seasonal and inter-annual variations) and detailed comparisons over specific regions.

5 ACKNOWLEDGEMENTS

The authors wish to acknowledge the following data sources: ECMWF for supplying the ERA-40 reanalysis data; ISCCP data were obtained from the NASA Langley Research Center Atmospheric Science Data Center. LL Lim, DS Lee and R Ismail acknowledge funding by the UK Department of Transport.

REFERENCES

Chen, C.T., and E. Roeckner, 1997: Cloud simulations with the Max-Planck-Institute for Meteorologie general circulation model ECHAM4 and comparison with observations. *J. Geophys. Res*. *102*, 9335-9350.

Penner, J.E., Lister, D.H., Griggs, D.J., Dokken, D.J., and McFarland, M. (eds.), 1999: *Aviation and the Global Atmosphere*. Intergovernmental Panel on Climate Change (IPCC), Cambridge University Press, UK. 373 pp.

Ovarlez, J., P. van Velthoven, G. Sachse, S. Vav, H. Schlager, and H. Ovarlez, 2000: Comparison of water vapor measurements from POLINAT2 with ECMWF analyses in high-humidity conditions. *J. Geophys. Res*. *105*, 3737-3744.

Rossow, W.R., A.W. Walker, D.E. Beuschel, and M.D. Roiter, 1996: *International Satellite Cloud Climatology Project (ISCCP) documentation of new cloud datasets*. Science Systems and Applications Inc. at NASA Goddard Institute for Space Studies.

Sausen, R., K. Gierens, M. Ponater, and U. Schumann, 1998: A diagnostic study of the global distribution of contrails Part 1: Present day climate. *Theor. Appl. Climatol*. *61*, 127-141.

Sundqvist, H., 1978: A parameterization scheme for non-convective condensation including prediction of cloud water content. *Q. J. R. Meteorol. Soc. 104*, 677-690.

Walcek, C.J., 1994: Cloud cover and its relationship to relative humidity during a springtime midlatitude cyclone. *Monthly Weather Review 122*, 1021-1035

Simulation of Contrails in the vortex regime – Examination of the microphysical properties

S. Unterstrasser*, K. Gierens
DLR-Institut für Physik der Atmosphäre Oberpfaffenhofen, Germany

P. Spichtinger
ETH Zürich-Institut für Atmosphäre und Klima, 8092 Zürich, Switzerland

Keywords: Contrails, Numerical modelling

ABSTRACT: In the vortex regime the contrail development is governed by the wake dynamics. The major fraction of the ice crystals is trapped inside the downward travelling vortex pair. For ambient supersaturations below a certain threshold, none of the trapped crystals survive the vortex phase. Only crystals detrained during the descent form the contrail. The ambient relative humidity has a strong impact on the vertical extent of the contrail and on the number of surviving ice crystals, especially in the vortex. Contrail development during the vortex regime was modelled with ambient supersaturations ranging from 0% to 20%. The computationally cheap 2D-code permits a large number of simulations. A realistic vortex decay was ensured using parameterisations of 3D-simulations. The obtained results give detailed information on initial states for contrail-to-cirrus simulations.

1 INTRODUCTION

Contrails form when the Schmidt-Appleman criterion is fulfilled (Schumann, 1996). Contrails are persistent when the surrounding air is supersaturated with respect to ice. During the vortex phase the majority of the ice crystals is trapped in the counter-rotating vortex pair and is transported downwards. Inside the descending vortices, adiabatic compression/heating reduces the relative humidity and leading eventually to the sublimation of ice mass (Sussmann and Gierens, 1999; Lewellen and Lewellen, 2001). The final vertical displacement depends on the initial strength of the vortex (aircraft parameter) and on its decay (controlled by meteorological parameters like turbulence, stratification). We identify the parameters which predominantly control the number and the distribution of ice crystals surviving the vortex phase. The main parameter discussed here is relative humidity. Further important parameters are flight level (i.e. temperature), initial circulation, turbulence, stratification, aircraft parameters (their is effect is not discussed here).

2 MODEL DESCRIPTION AND SETUP

The large-eddy simulations have been carried out with the non-hydrostatic anelastic 3D model EULAG (Smolarkiewicz and Margolin,1997) which was supplemented with an ice microphysics code (Spichtinger, in prep). The parameterised microphysical processes are deposition growth/ condensation and sedimentation. The simulations run on a 2D domain. The horizontal direction x is along wingspan and z is the vertical coordinate. The domain has an horizontal/vertical extent of x_D=256m and z_D=500m with 1m-resolution in each direction. The time step is dt=0.02s. The simulations start at the beginning of the vortex phase and end with vortex break-up after 135s. The aircraft properties typical of a large aircraft are implemented (initial circulation $\Gamma_0 = 650$ m²/s, wing span bspan=60m). The ice crystals are uniformly distributed in circles (r=20m) around the vortex

* *Corresponding author:* Simon Unterstrasser, DLR-Institut für Physik der Atmosphäre, Oberpfaffenhofen, D-82205 Wessling, Germany. Email: simon.unterstrasser@dlr.de

centres. The total emitted water (1.46 10^{-2} kg per m flight path) is contained in the ice crystals (3.4 10^{12} per m flight path). Furthermore, the nucleation of the ice crystals is assumed to be completed during the jet phase and no further nucleation is considered during the vortex phase. The temperature at cruise altitude is 222K. The pressure is p_0=250hPa at the lower boundary. The atmosphere is stably stratified (Brunt-Väisälä frequency $N=10^{-2}s^{-1}$) with an initially constant relative humidity with respect to ice. The supersaturation s_i ranges from 0% to 20%. The eddy dissipation rate is 3.5 10^{-5} m^2 s^{-3}

3 VORTEX DYNAMICS

The decay of the vortex pair depends on meteorological parameters (stratification and eddy dissipation rate) as well as on aircraft parameters (initial circulation Γ_0 and initial vortex separation b_0).
The vortex decay can be divided into two regimes. During the diffusion phase the vortex weakens independently of the latter parameters. After a certain onset time T2 the rapid decay phase sets in.
Generally, time T2 is smaller and the rapid decay is faster for higher turbulence and for stronger stratification. The temporal evolution of Γ in dependence of the parameters mentioned above is given in Holzäpfel, 2003 (see Fig. 1, solid line).
In 2D-simulations the vortex decay is generally too slow as the Crow instability (the most efficient destructive process) is not resolved (see Fig. 1, dashed line). The diffusion coefficient in the simulations is artificially increased around the vortex cores and adapted each second in order to assure a realistic decay. The simulated circulation (see Fig. 1, dotted line) is in good agreement with the values given in Holzäpfel, 2003.

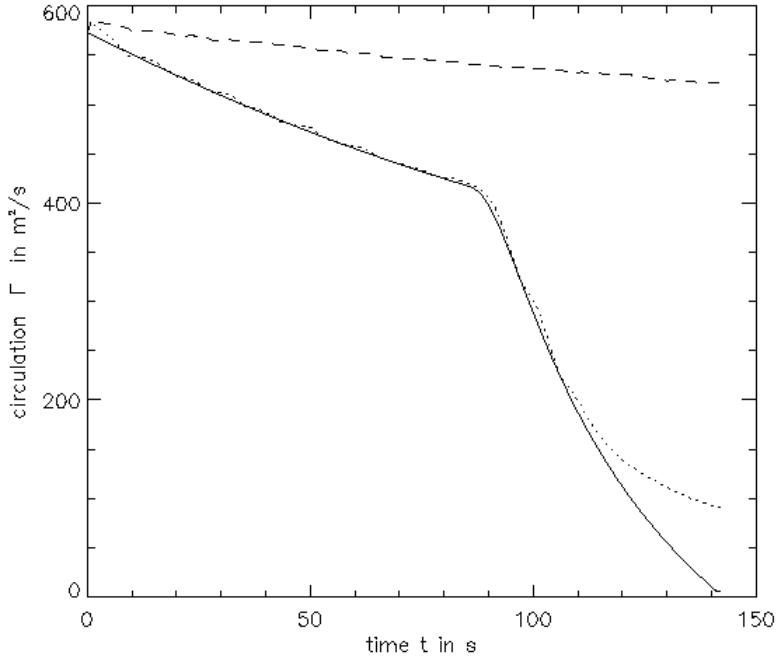

Figure 1: Temporal evolution of the circulation Γ

4 RESULTS

The total ice mass per flight path tIWC [kg/m] is computed with the following integral.

$$tIWC = \iint IWC(x,z)dxdz$$

In order to determine the ice mass contained in the primary wake pIWC, the integral is restricted to 40m-circles around the vortex centres. The area of the secondary wake is one 50m-circle centred at the flight altitude in the middle of the domain (i.e the position that was crossed by the body of the aircraft). The according integral quantity is called sIWC. Analogously, the number of ice crystals in the different areas (tN,pN,sN) is determined. In some figures, the latter quantities are normalised by

the initial ice mass or crystal number, resp. These quantities tell us which fraction of ice mass and crystals is still present after a certain time. In general, the contrail loses a major part of its crystals in the primary wake. At the beginning of the simulation, the areas of the primary and the secondary wake overlap. At later times, there is a vertical gap, as the vortex pair travelled downwards. The amount of ice in the so-called curtain (i.e. the vertical stripe between the vertically displaced vortex and flight altitude) can be determined by tIWC-pIWc-sIWC.
The temporal evolution of the normalised quantities is shown in Figure 2. The temperature at cruise altitude is T_{CA}= 222K and the relative humidity RH_i is 105%.

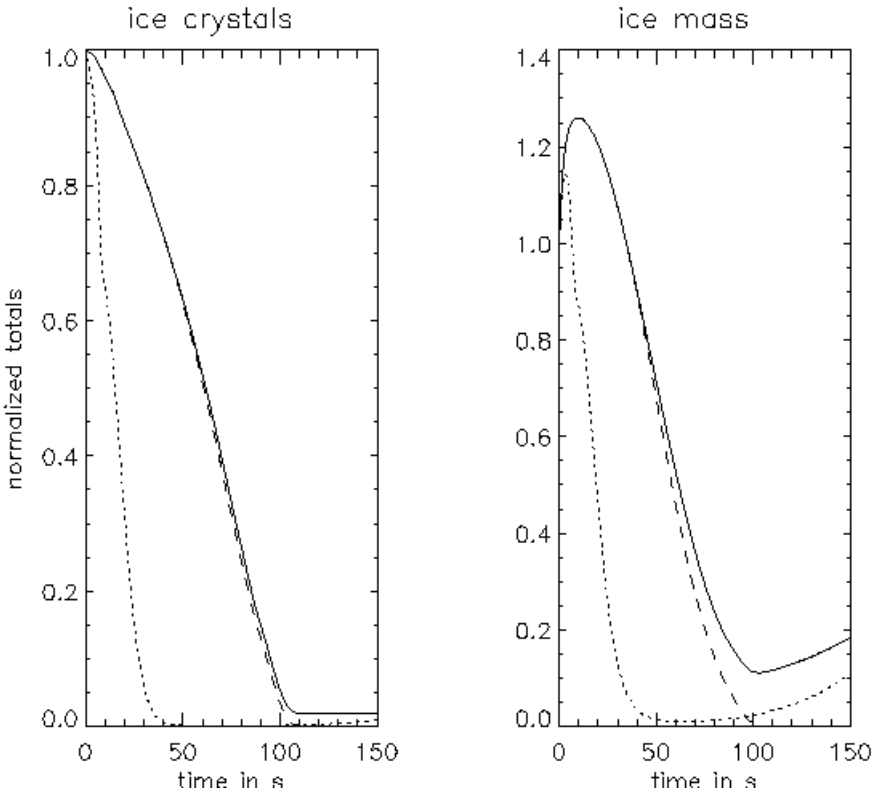

Figure 2: left panel: temporal evolution of the number of ice crystals in the total area tN (solid line),in the primary wake pN (dashed line) and in the secondary wake sN (dotted line). Right panel: Analogously for ice mass. The ambient supersaturation was 5%.

Initially, tIWC increases due to deposition growth of the ice crystals until the excess moisture from ambient supersaturation is consumed. During the downward transport the local RH_i in the vortices decreases due to adiabatic heating and the number of ice crystals declines in the primary wake. Later the minor number of crystals in the secondary wake becomes significant, as these crystals steadily grow. Figure 3 shows the vertical profiles of ice mass and crystals at vortex break-up time t=135s. The profiles are shown for various relative humidities (100%, dotted; 105% dashed; 110% dash-dotted; 120% dash-dot-dotted). Again, the temperature is 222K.
The initial ice crystal distribution was centred around z=400m (solid line). After 135s the vortex pair travelled below z=200m. A substantial fraction of the trapped ice crystals survives only for high supersaturation ($s_i \geq 10\%$). This threshold s_i-value depends on vortex break-up time, descent speed and temperature. It can be concluded that the mean ice crystal mass in the primary wake is smaller than in the secondary wake at the end of the vortex phase. The earlier the crystals are detrained and mix with ambient air, the larger they are. The moister it is, the larger is the vertical extent of the contrail and the more ice crystals survive the vortex phase.

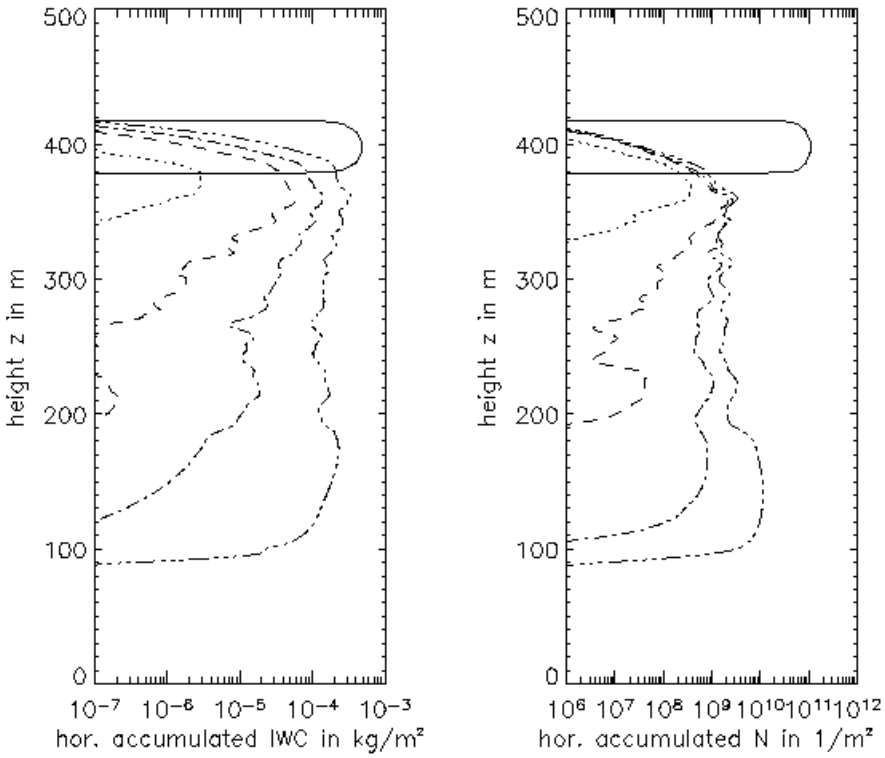

Figure 3: vertical profiles of ice mass (left) and crystals (right) for various supersaturations s_i (0%, dotted; 5% dashed;10% dash-dotted; 20% dash-dot-dotted).

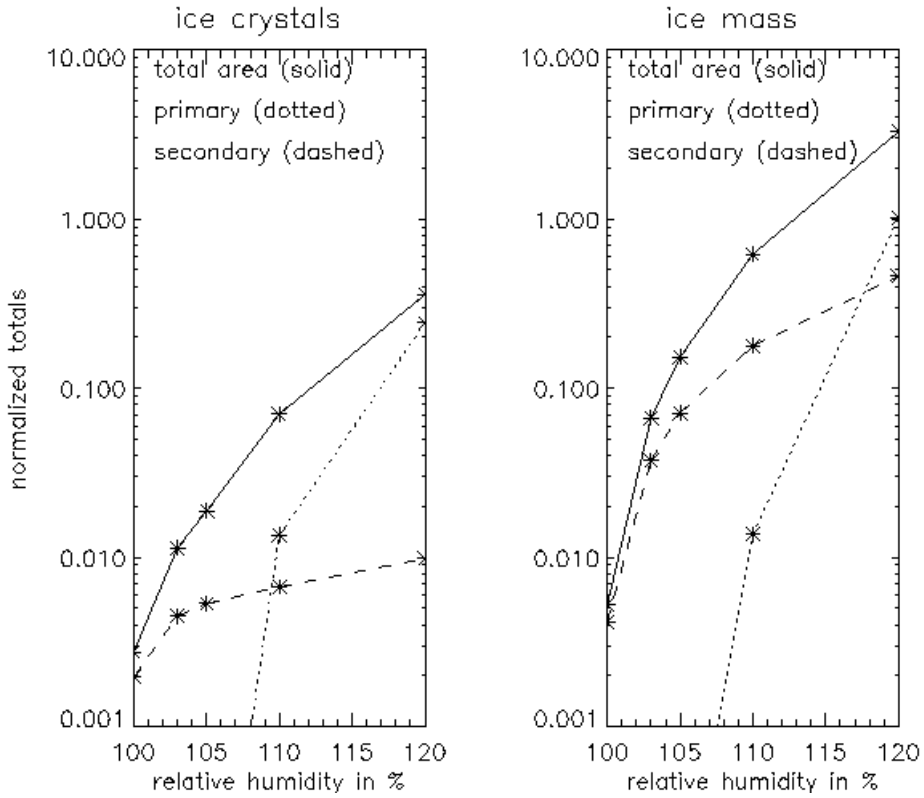

Figure 4 left panel: Normalised totals of surviving ice crystals tN,pN and sN as a function of RH_i. Analogously, the surviving ice mass on the right hand side.

Figure 4 shows the normalised totals of ice mass/crystals at the time of vortex break-up as a function of RH_i. In all cases, the normalised number of surviving crystals is below unity. Not surprisingly, a moister environment is favourable for less ice crystal loss. The normalised tN ranges from 40% at s_i =20% to less than 1% at s_i =0%. The number of ice crystals in the secondary wake sN is

weakly dependent of humidity and nearly all crystals which were not trapped inside the initial vortex pair survive, as long as the ambient relative humidity $RH_i \geq 100$. Generally, the fraction of crystals in the secondary wake increases relative to the primary wake with decreasing supersaturation. The right panel of Figure 4 shows the normalized value of surviving ice mass. It is apparent, that the ice mass in the secondary wake increases with relative humidity, as more excess moisture condenses on the crystals. At high supersaturation a major part of the ice mass is inside the secondary wake, although less than 1% of the crystals are detrained in the beginning.
At vortex breakup time, the total ice mass and number of crystals present as a function of RH_i can be fitted with a power law $a \cdot (RH_i - b)^{\alpha}$. The exponent α is roughly 3 for the present simulations, but it may depend on other meteorological variables.

5 CONCLUSION/ACKNOWLEDGEMENTS

Relative humidity was identified as one key parameter for the microphysical properties of a contrail at the end of the vortex phase. The number of surviving ice crystals grows with supersaturation. In cases with $RH_i \leq 110\%$, the total IWC after 135s was below the initial level. The vertical profile of the ice crystal distribution strongly depends on RH_i and the concentration and the mass of the crystals is different for the primary and secondary wake. Many more parameters (as given in the introduction) can be studied with the existing code. Especially, the variation of temperature has also an major impact on the contrail properties. The presented results will be used as initial states for simulations of the dispersion phase. This will help to understand and simulate the contrail-to-cirrus transformation.
We want to thank Andreas Dörnbrack for help with EuLag and for many fruitful discussions. We further acknowledge stimulating discussions with Bernd Kärcher, Thomas Gerz and Frank Holzäpfel. The simulations were carried out on the high computing facilities at the ECMWF (special project “Ice supersaturation and cirrus clouds”).

REFERENCES

Lewellen, D.C., W.S. Lewellen, 2001: The effects of Aircraft wake Dynamics on Contrail Development, *J Atmos. Sci.*, 58, 390-406

Schumann, U., 1996:, On conditions for contrail formation from aircraft exhausts, *Meteor. Z.*, 5, 4-23

Smolarkiewicz, P.K., G.Margolin, 1997: On Forward-in-time Differencing for Fluids: An Eulerian/Semi-Lagrangian Non-hydrostatic Model for Stratified Flows, *Atmos. Ocean Special*, 33, 127-152

Sussmann, R., K. Gierens, 1999: Lidar and numerical studies on the different evolution of vortex pair and secondary wake in young contrails, *J. Geophys. Res,* 104, 2131-2142

Homogeneous freezing of ice particles, including effects of aerosol size distribution in the University of L'Aquila CCM

G. Pitari*, D. Iachetti and V. Montanaro
Department of Physics, University of L'Aquila, Italy

Keywords: homogeneous freezing, aerosol size effects.

ABSTRACT: The numerical code developed by Kärcher and Lohmann [*JGR 2002*], for the parametrization of cirrus cloud formation via homogeneous freezing of supercooled aerosols is introduced on-line in the climate-chemistry coupled model of the University of L'Aquila (ULAQ-CCM). In this paper we briefly describe the parameterization adopted and the model results for the basic quantities (updraft velocities, particle size distributions, top of the atmosphere radiative fluxes). A future application will be to calculate the radiative forcing due to ice particle perturbations produced by aircraft induced changes of the aerosol size distribution.

1 INTRODUCTION.

A low resolution climate-chemistry coupled model, including a microphysics code for aerosols formation and growth, is used to study ice particle formation in cirrus clouds, including the effects of the aerosol size distribution. The parameterization used is that for homogeneous freezing of supercooled aerosols of Kärcher and Lohmann [*JGR 2002a*], extended to include the effects of aerosol size on the freezing process in adiabatically rising air particles [*Kärcher and Lohmann, JGR 2002b*]. Homogeneous freezing is considered as the most important ice formation mechanism under upper tropospheric conditions. The adiabatic cooling due to the vertical ascent rate is the key parameter determining the population of ice particles (number density and radius). For this reason, in order to have a realistic representation of small-scale freezing, the vertical velocities field used in the ice-formation code is the sum of the large scale vertical velocity (almost negligible) and a small-scale term, calculated as a function of the turbulent kinetic energy. Changes of the aerosol size distribution can modify the homogeneous freezing process when the timescale of the freezing event is fast (low temperatures and high vertical velocities).

We present here the results of the ULAQ-CCM about the feedback of the aerosol size distribution on the mechanism of formation and growth of ice particles in the UT/LS region, obtained with the two parameterizations (with/without impact of theaerosol size distribution). We also show preliminary results on the top of atmosphere radiative fluxes due to ice cloud particles in the UT/LS.

2 DESCRIPTION OF THE MODEL.

The ULAQ model is a low-resolution three-dimensional (3D) climate-chemistry coupled model (CCM). The chemical-transport module uses a 10°×22.5° grid in latitude-longitude (19 latitudes and 16 longitudes) and 26 log pressure levels, from the ground to about 0.04 hPa, with an approximate spacing of 2.84 km. Dynamical fields (streamfunction, velocity potential and temperature) are taken from the output of a spectral general circulation climate model GCM [*Pitari et al., JAS 2002*], which is in turn coupled to the CTM via the radiatively active species (O_3, H_2O, WMGHGs and aerosols). The vertical velocity is calculated from the horizontal divergence. A flux-form Eulerian fully explicit advection scheme is used, with 1 h time step, used for both dynamics and chemistry. Relative humidity, warm cloud distribution and net precipitation rates are taken from climatological data. A vertical diffusion coefficient K_{zz} is used to simulate those transport processes not explicitly included in the model. The scheme adopted for tropospheric deep convection takes inspiration from

* *Corresponding author:* Giovanni Pitari, Università degli Studi de L'Aquila, Dipartimento di Fisica, via Vetoio, 67010 Coppito, L'Aquila, Italy. Email: gianni.pitari@aquila.infn.it

that described in Muller and Brasseur [*JGR 1995*]: the rate at which a chemical compound is transported at a given altitude in the free troposphere is calculated as a function of a convective uplift rate and the species mixing ratio in the boundary layer.

The main removal processes of aerosol particles parameterized in the model are wet deposition, dry deposition and sedimentation. ULAQ model includes the major components of tropospheric aerosols (sulphates, carbonaceous, soil dust, sea salt). Aerosol particle are divided in size bins and each one is separately transported. Surface fluxes of SO_2 , DMS, black carbon, organic carbon and mechanically generated particles are those provided for Experiment B of the AEROCOM international assessment campaign [*Textor et al., ACP 2006*].

The parameterization of homogeneous freezing by Kärcher and Lohmann [*JGR 2002a and 2002b*], (K & L hereafter) was derived from first principles, based on the supersaturation and ice crystal growth equations. In contrast to previous parameterizations, this scheme considers the basic physical processes that eventually determine the number of ice crystals N_i forming during an adiabatic ascent, including the dependences of N_i on temperature and updraft speed. In particular, it was found that this dependence is quite insensitive to details of the aerosol size distribution in many cases, but increases rapidly with updraft velocity and decreases with temperature. In the reference simulation HOM, the number of frozen ice crystals formed via homogeneous freezing, at temperatures below 235 K is obtained as:

$$N_i^{HOM} = \min\left[\frac{m_\omega}{\rho_i}\left(\frac{b_2}{2\pi b_1}\right)^{\frac{3}{2}}\frac{a_1 S_{cr}}{a_2 + a_3 S_{cr}}\cdot\frac{\omega}{\sqrt{\tau}}; N_a\right] \quad (1)$$

where m_ω is the molecular weight of water, ρ_i is the ice crystal density (=925 kg m^{-3}), S_{cr} is the critical supersaturation ratio, where freezing starts, ω is the updraft velocity, $\tau \propto 1/\omega$ is the characteristic time scale of the nucleation event and a_1, $a_2=1/N_{si}$, a_3, $b_1 \propto N_{si}\,(S_{cr}-1)$, b_2 are temperature-dependent variables, N_{si} denotes the water vapor number density at ice saturation, depending on temperature. Note that the nucleation rate is limited by the number of hygroscopic aerosol particles N_a defined as:

$$N_a = N_{seasalt} + N_{BC}^{phil} + N_{OC}^{phil} + N_{dust} + N_{SO_4} \quad (2)$$

If the effects of the aerosol size are not taken into account, one can deduce the approximate scaling relationship :

$$N_i^{HOM} \propto \omega^{3/2} N_{si}^{-1/2} \quad (3)$$

The mesoscale updraft velocity ω is obtained as the sum of the large scale vertical velocity and a small scale term, calculated as a function of the turbulent kinetic energy TKE [*Abdella and McFarlane, JGR 1997*]:

$$\omega = \overline{\omega} + 0.7\sqrt{TKE} \quad (4)$$

In deriving (3), K & L argued that aerosol size effects on the homogeneous freezing process are unimportant whenever the initial growth time scale of ice particles is shorter than the time scale of the nucleation event (fast growth regime). Here the number of ice crystals is independent of the initial aerosol size.

Aerosol size effects (simulation HOM-Size) are important in the slow growth regime, characterized by high vertical velocities and cold temperatures; the freezing growth term becomes considerably more complicated. Assuming a monodisperse aerosol particle size distribution:

$$N_i^{HOM-Size} \propto a_1 S_{cr}\cdot\omega\cdot\frac{N_{si}}{R_{i,m}(r_0)} \quad (5)$$

where $R_{i,m}(r_0)$ is the monodisperse freezing/growth integral explained by K & L, that depends on the initial particle radius r_0. The parameterization scheme considers a multimodal aerosol size structure, with four modes, each one characterized by a lognormal distribution curve. Consequently, the parameterization is called by the ULAQ model with the mean radius, number density and geometric width for each mode.

Short wave (SW) top of the atmosphere radiative fluxes are calculated as the top-of-atmosphere solar flux changes due to ice crystals, using a multi-layer δ-Eddington approximation. To evaluate long wave (IR) fluxes, we use pre-calculated tropopause IR fluxes, scaled with appropriate σT^4 for absorption/emission, as described in Lacis and Hansen [*JRL 1992*]).

3 RESULTS AND DISCUSSION.

The simulations were conducted over a period of 5 years after an initial spin-up of 5 years using climatological sea surface temperature (Hadley Center data). As the reference simulation HOM does not take into account the effects of aerosol size, the simulation HOM-Size includes aerosol size effects.

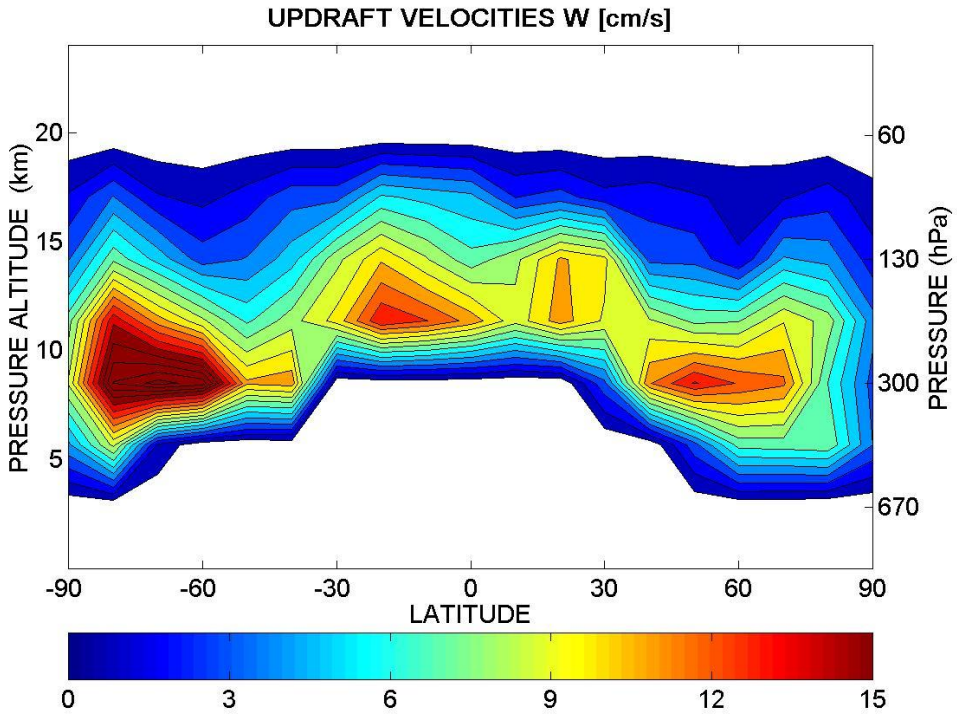

Figure 1: zonally and annually averaged background updraft velocities [cm/s].

Figure 1 shows the mesoscale updraft velocities calculated in the model as a function of the turbulent kinetic energy: typical values in the upper troposphere are in the 10÷15 cm/s range. As shown by K & L [*JGR 2002a*], the vertical velocities play a critical role for the adiabatic cooling and the formation of ice crystals. The expected number density and size of the particles are 0.1÷1 cm^{-3} and 3÷20 μm, respectively. This is confirmed by the calculated ice crystal number and mass density size distributions shown in Figure 2.

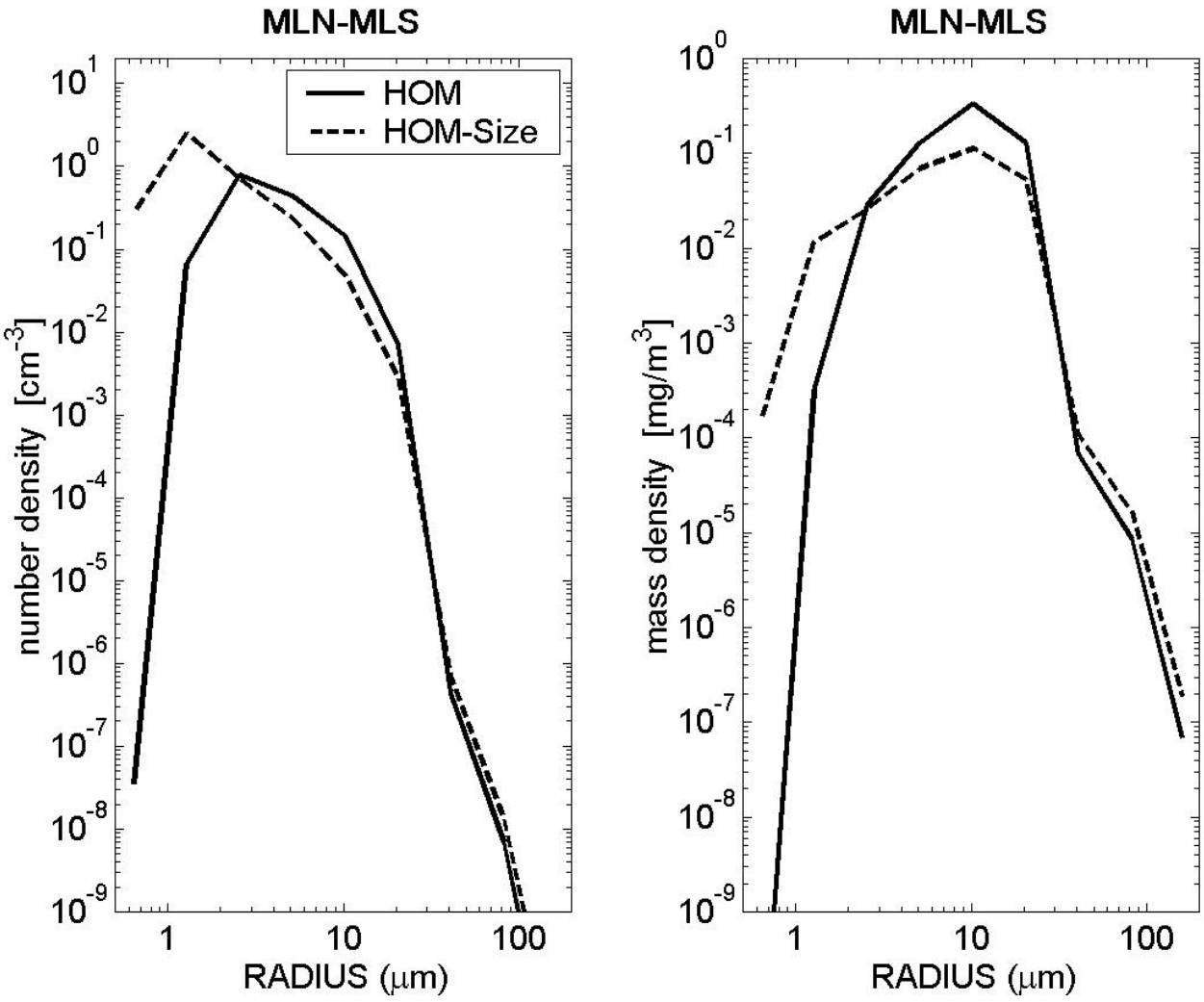

Figure 2: ice crystals number density [cm^{-3}] and mass density [mg m^{-3}] size distributions at mid latitudes (average of Northern Hemisphere (MLN) and Southern Hemisphere (MLS) values). Solid and dashed lines are for HOM and HOM-Size simulations, respectively.

Here we see that the effects of the aerosol size distribution is to increase the number density of particles smaller than 3 μm. For this reason the difference HOM-Size – HOM gives an increase of the total number concentration of ice crystals (1÷5 cm^{-3}), as shown in Figure 3.

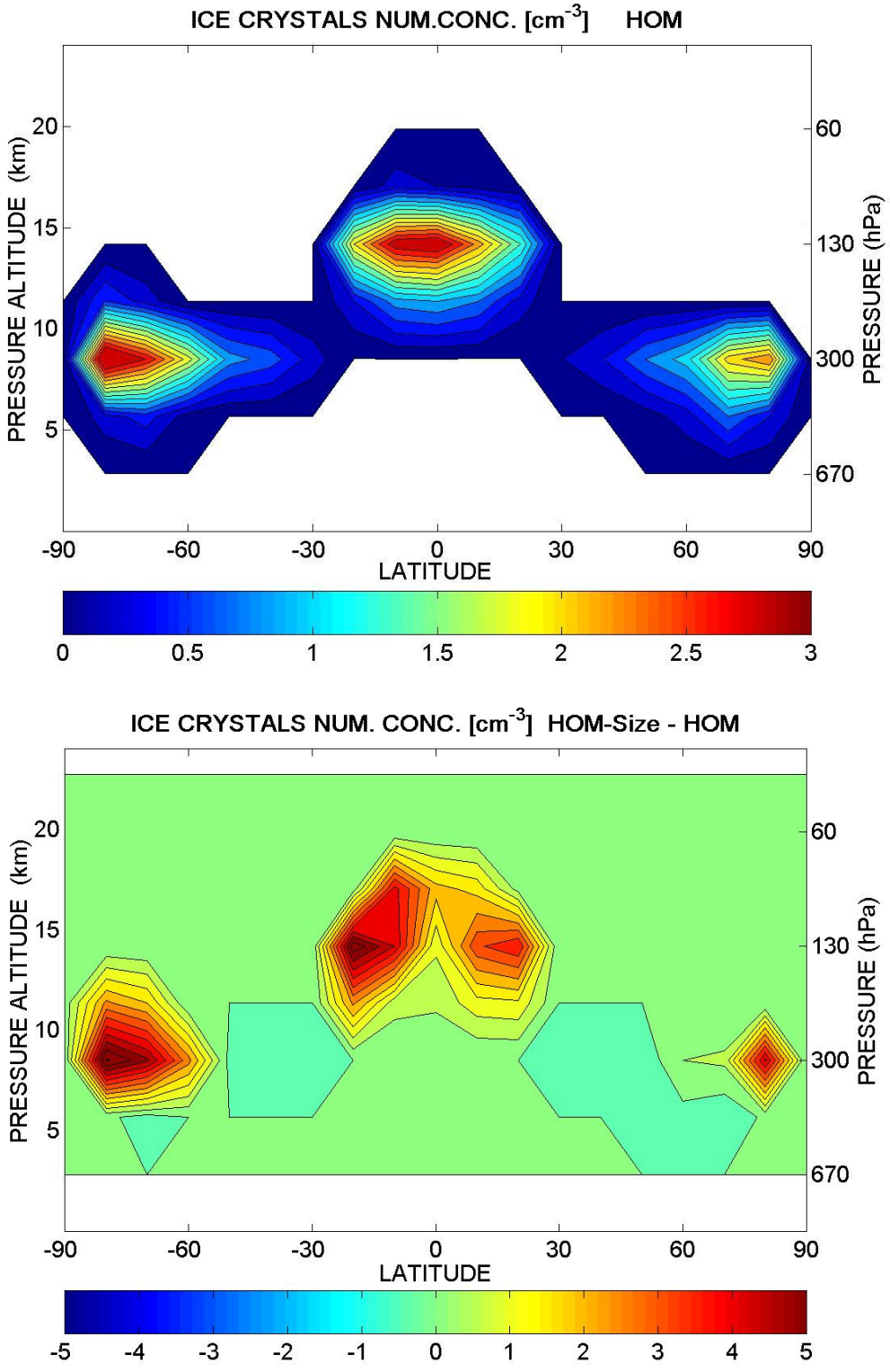

Figure 3: zonally and annually averaged ice crystals number densities for simulation HOM (top panel) and the difference between simulations HOM-Size and HOM (bottom panel), [cm^{-3}].

The key role of the vertical ascent rate for the adiabatic cooling and water vapour freezing is clear when comparing Figure 1 and 3a.

A preliminary calculation of radiative flux changes due to ice particles is presented in Figure 4. Additional refinements are needed here for the infrared fluxes (since we use pre-calculated fluxes of IR absorption/emission) which are appropriate for H_2O-H_2SO_4 mixtures.

These radiative calculation will soon be used to estimate the radiative forcing produced by ice particle size distribution changes due to aircraft induced aerosol size distribution perturbations.

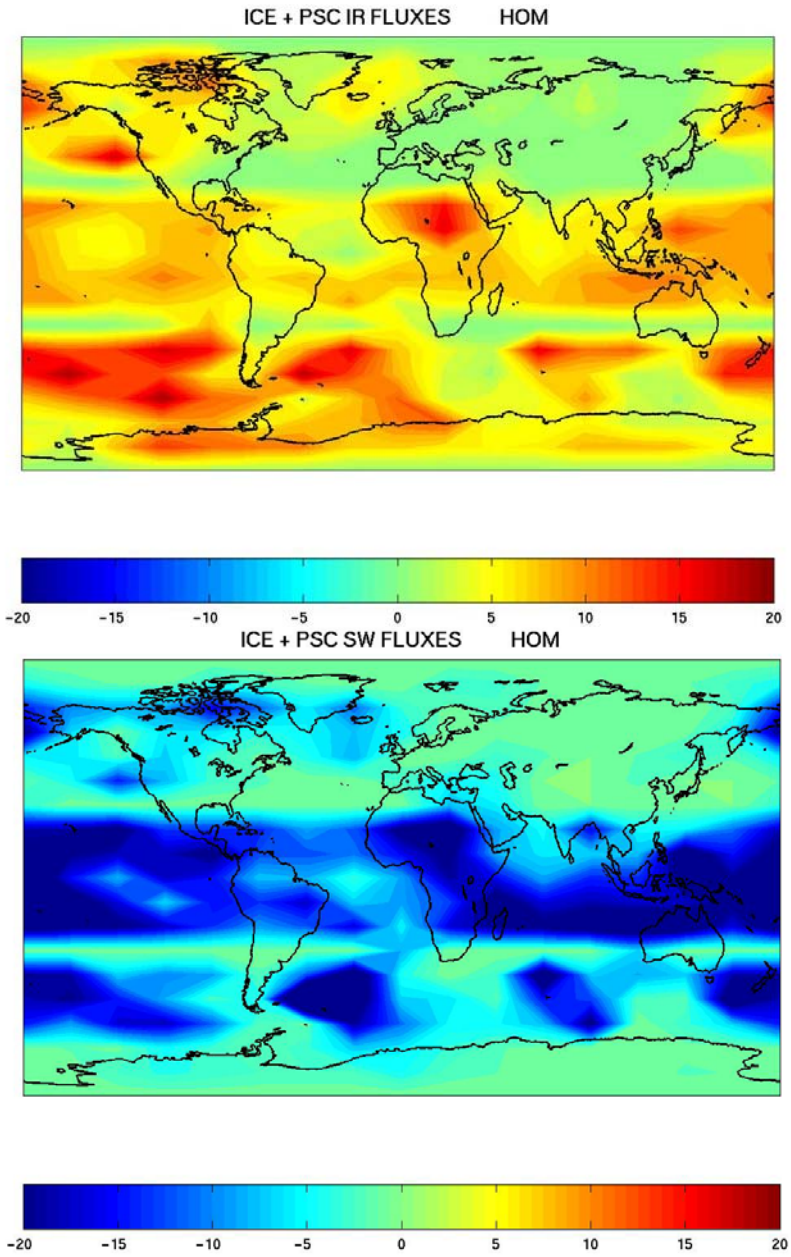

Figure 4. Geographical distribution of annually averaged top of the atmosphere IR fluxes (top panel) and solar fluxes (bottom panel), due to ice particles in the UT/LS [mW/m^2]. Results are for the simulation HOM.

REFERENCES

Abdella K. , and N. McFarlane, 1997: A new Second order turbulence closure scheme for the planetary boundary layer, *J. Geophys. Res.*, *54*, 1850 – 1867.

Kärcher, B., and Lohmann, U., 2002a: A parameterization of cirrus cloud formation: homogeneous freezing of supercooled aerosols, *J. Geophys. Res.*, *107*, 4010, 10.1029/2001JD000470.

Kärcher, B., and Lohmann, U., 2002b: A parameterization of cirrus cloud formation: homogeneous freezing including effects of aerosol size, *J. Geophys. Res.*, *107*, 4698, 10.1029/2001JD001429.

Lacis, A., J. Hansen, and M. Sato, 1992: Climate forcing by stratospheric aerosols. *Geophys. Res. Lett.,* 19, 1607-1610.

Muller, J.-F. and G. Brasseur, 1995: A Three Dimensional Transport Model of the Global Troposphere, *J. Geophys. Res.*, *100*, 16445 – 16490.

Pitari, G., E. Mancini, V. Rizi, and D. T. Shindell, 2002: Impact of future climate and emissions changes on stratopsheric aerosola and ozone, *J. Atmos. Sci.*, *59*, 414-440.

Textor, C., M. Schultz et al., 2006: Analysys and quantification of the diversities of aerosol life cycles witin AeroCom, *Atmos. Chem. Phys.*, *6*, 1777-1813.

Calculating contrail radiative forcing with the Edwards-Slingo radiative transfer code

R. Rodriguez De León*, D. S. Lee
Dalton Research Institute, Department of Environmental and Geographical Sciences, Manchester Metropolitan University, UK

Keywords: radiative transfer, optical properties, ice crystals, particle size distribution, hexagonal cylinders

ABSTRACT: The Edwards-Slingo radiative transfer code has been used to examine the radiative forcing that might arise from contrails. A set of conditions as used by Meerkötter et al. (1999) provided a convenient benchmark for the results. The assumption of a hexagonal cylinder habit was tested with the Edwards-Slingo code and compared to Meerkötter et al.'s (1999) spheroidal approximation to hexagonal cylinders. Overall, a more realistic assumption of hexagonal crystals resulted in a smaller net forcing than if spherical particles or spheroidal approximations are assumed.

4 INTRODUCTION

Persistent line-shaped contrails induced by air traffic have been estimated to cover at least 0.5% of central Europe's skies at noon (Mannstein et al., 1999). Under favourable temperature and humidity conditions, these clouds can expand in their vertical and horizontal extent to become contrail-cirrus, potentially increasing their influence on the planet's radiative balance (IPCC, 1999; Stordal et al., 2005). Meerkötter et al. (1999) (hereafter M99) found that in all the relevant study areas contrails enhance the "greenhouse effect" because they reduce outward longwave fluxes more than they increase reflected shortwave fluxes. The balance between these opposite effects depends upon the characterization of macro- and micro-physical properties of contrails, which represents a significant challenge for both measurements and theoretical modelling.

The microphysical properties of young contrails are likely to depend in a non-trivial way on the dynamics and thermodynamics of the atmosphere-engine system. Line-shaped contrails, like young cirrus, are mostly composed of small particles, which do not deviate largely from a spherical geometry; but as a persistent contrail ages, its particles may acquire more complex non-spherical habits.

In this study the Edwards-Slingo (E-S) radiative transfer code (Edwards and Slingo, 1996) was used for the first time to study contrails by incorporating into it a new radiative parameterization based on the optical properties of hexagonal cylinders. The instantaneous or static radiative forcing of a 200 metres contrail layer is presented and compared with M99's results.

5 METHODOLOGY

As a guiding principle, we use the model conditions described by Meerkötter et al. (1999) since they used three different radiative transfer codes and provided a useful 'benchmark' which includes seven cases for the cloud's microphysics (particle size), macrophysics (cloud ice water content, cloud thickness and cloud height) and the environment's physics (seasonal temperature profile and surface albedo). Following M99, the simulations were run to calculate the daily mean (24 h) net

* *Corresponding author:* Rubén Rodríguez De León, Department of Environmental and Geographical Sciences, Faculty of Science and Engineering, John Dalton Building, Chester Street, Manchester, M1 5GD. Email: r.deleon@mmu.ac.uk

forcing caused by a 200 metres thick contrail layer. We used hexagonal cylinders as a representative habit, for which the optical properties were taken from Yang et al. (2000) in the shortwave (SW) and from Baran et al. (2002) in the longwave (LW) regions of the spectrum.

In the following section our results for hexagonal cylinders are compared with M99's results for equivalent spheroids and equivalent spheres using his suggested contrail size distribution, corresponding to a generalized size (Fu, 1996) of 29.2 micrometres.

Table 1. Daily mean (24 h) radiative flux changes at the top of the atmosphere (TOA, 50 km) in W m-2 for hexagonal cylinders (first entry) integrated over Strauss et al's (1997) contrail size distribution. For comparative purposes the calculations from Meerkötter et al. (1999) for spheroids and spherical particles are also presented (second and third entries).

Region	Albedo	IWC	Cloud Top (km)	Shape	Effective size (microns)	SW Wm^{-2}	LW Wm^{-2}	NET Wm^{-2}
a) Midlatitude summer continent 45°N	0.2	21	11	Hex-cyl Spheroids Spheres	29.2 29.2 29.2	-18.7 -22.0 -13.4	38.4 51.5 51.6	19.7 29.5 38.2
b) Midlatitude winter continent 45°N	0.2	7.2	11	Hex-cyl Spheroids Spheres	29.2 29.2 29.2	-5.5 -4.6 -4.2	9.6 18.3 18.4	4.0 13.7 14.2
c) Midlatitude winter continent with snow, 45°N	0.7	7.2	11	Hex-cyl Spheroids Spheres	29.2 29.2 29.2	-2.6 -2.0 -2.3	9.6 18.3 18.4	7.0 16.3 16.1
d) North Atlantic summer ocean 55°N	0.05	21	11	Hex-cyl Spheroids Spheres	29.2 29.2 29.2	-21.1 -32.7 -21.5	38.4 50.9 53.3	17.2 18.2 31.8
e) Tropical ocean (Equator, June)	0.05	23	11	Hex-cyl Spheroids Spheres	29.2 29.2 29.2	-27.6 -25.9 -16.0	51.8 57.4 63.0	24.2 31.5 47.0
f) Subarctic summer ocean 62°N	0.05	28.2	9	Hex-cyl Spheroids Spheres	29.2 29.2 29.2	-45.8 -45.3 -30.8	38.6 49.1 55.7	-7.2 3.7 24.9
f) Subarctic winter ocean ice 62°N	0.7	7.2	9	Hex-cyl Spheroids Spheres	29.2 29.2 29.2	-0.7 -0.7 -0.6	8.9 13.2 14.6	8.2 12.5 14.0

6 RESULTS

The calculated shortwave (SW), longwave (LW) and net (SW+LW) radiative forcings arising from a 200 metres thick contrail layer represented by hexagonal cylinders are presented in Table 1 (top entry of each row) together with M99's results for spheroids and spheres (second and third entries, respectively). All cases were calculated using the contrail particle size distribution suggested by M99 (e.g. Strauss et al., 1997) corresponding to a generalized size (Fu, 1996) of 29.2 microns. The differences are only linked to the particle shape adopted and show that the LW forcing is proportional to the particle's sphericity. Given this proportionality and the fact that any other shape will represent an intermediate case between a sphere and a column, it is understood that any other habit used as a representative shape to model contrails will produce net forcings between the values

given by our hexagonal cylinder and M99's spherical calculations. The spherical case was chosen by M99 as their best estimate, but given that the purpose of our study is to find representative forcings for persistent contrails, it seem sensible to consider values closer to the hexagonal case than to the spherical one.

The contrail RF is influenced by the latitude in various ways, in the SW through the daytime length, in the LW through the humidity profile and the temperature difference between the surface, and in both cases through the altitude at which the necessary conditions for contrail formation are met. Taking into account all these factors it is not unexpected to obtain differences in the net RF between cases d) and f), both with summer-ocean conditions but with different latitude profiles, cloud heights and ice water contents. These differences are important because for the hexagonal calculations they produce a negative net forcing in the subarctic region, which was not predicted when applying the other habits. Using an IWC value equal to 21 mg m^{-3} in case f) produces 30.4 (LW), -36.2 (SW) and –5.8 (NET) Wm^{-2} forcings, showing that the height of the contrail and atmospheric profile in which we place it have a larger influence on the sign of the net forcing than the IWC.

7 CONCLUSIONS

The E-S radiative transfer code has been shown to be suitable for undertaking calculations of contrail radiative forcing. The results are sensitive to the assumptions about the representative shape and size distribution of contrail particles, which may depend on the contrail's age. Hexagonal cylinders present smaller LW forcings, which translate in smaller net forcings, and may become negative at high latitudes with small albedos

On balance, it would seem more realistic to use the hexagonal parameterization facilitated by the E-S model in both SW and LW domains; the results obtained here would indicate a smaller net forcing than if spherical particles are assumed.

Future work will focus on integrating these results into a global model of the impact of contrails on the planet's radiative balance.

REFERENCES

Baran, A. J., S. Havemann, and D. Mackowsky, 2002: A database of hexagonal column optical properties for wavelengths ranging between 0.2 to 30 microns produced for ANNEX, Contract no 4b/3/02, DEFRA, UK.

Edwards, J. M., and A. Slingo, 1996: Studies with a flexible new radiation code. I: Choosing a configuration for a large-scale model. *Quarterly Journal of the Royal Meteorological Society, 122,* 689–719(31)

Fu, Q., 1996: An accurate parameterization of the solar radiative properties of cirrus clouds for climate models. *Journal of Climate, 9,* 2058-2082.

Fu, Q. and K. N. Liou, 1993: Parameterization of the radiative properties of cirrus clouds. *Journal of Atmospheric Science, 50,* 2008–2025.

IPCC, 1999: Aviation and the Global Atmosphere. J. E. Penner, D. H. Lister, D. J. Griggs, D. J. Dokken and M. McFarland (Eds). Special Report of the Intergovernmental Panel on Climate Change, Cambridge University Press, Cambridge.

Mannstein, H., R. Meyer, and P. Wendling, 1999: Operational detection of contrails from NOAA-AVHRR-data, *International Journal of Remote Sensing*, *20(8),* 1641–1660.

Meerkötter, R., U. Schumann, D.R. Doelling, P. Minnis, T. Nakajima, Y. Tsushima, 1999: Radiative forcing by Contrails. *Annales Geophysicae, 17,* 1080-1094.

Stordal F., G. Myhre, E. J. G. Stordal, W. B. Rossow, D. S. Lee, D. W. Arlander and T. Svenby T., 2005: Is there a trend in cirrus cloud cover due to aircraft traffic? *Atmospheric Chemistry and Physics 5*, 2155–2162.

Strauss, B., R. Meerkötter, B. Wissinger, P. Wendling, and M. Hess, 1997: On the regional climatic impact of contrails: microphysical and radiative properties of contrails and natural cirrus clouds. *Ann. Geophysicae, 13,* 1457–1467.

Yang, P., K. Liou, D. Wyser and D. Mitchell, 2000: Parameterization of the scattering and absorption properties of individual ice crystals. *Journal of Geophysical Research,105(D4),* 4699–4718.

Pedestrian exposure to vehicle emissions: the role of traffic signal timings

Muhammad M. Ishaque, R.B. Noland*
Imperial College London,UK

Keywords: pedestrian, micro-simulation, air quality, VISSIM, CMEM, CAL3QHC

ABSTRACT: This paper analyses pedestrian exposure to vehicle emissions and the role played by signal timings. A simple junction is coded in a micro-simulation model and time series data on vehicle performance, i.e., speed and acceleration is generated for various signal time settings. This data is then used to calculate vehicle emissions with a modal emissions model. The effects of these emissions on the pedestrian paths and crossings adjacent to the traffic junction are then estimated using an air dispersion model. The suitability of various traffic signal plans in terms of pedestrian exposure to harmful vehicular emissions is discussed.

1 INTRODUCTION

The present work is an endeavour to measure Carbon Monoxide (CO) exposure of waiting pedestrians at pedestrian crossings on a traffic intersection and the effect of different signal timings. The objective is to relate signal timings to pedestrian exposure in addition to pedestrian delay and is a continuation of research work by the authors analysing various MOE (measures of effectiveness) trade offs between vehicular and pedestrian traffic from changing traffic management policies. Previous work has shown that the signal timings designed to facilitate vehicle flow, minimising vehicle delay and providing only minimum time for pedestrians might not be the optimal solution when relative values of time are taken into account and pedestrian volumes are high (Ishaque and Noland, 2005a; 2005b). That work, however, did not consider vehicle emissions, to which pedestrians are exposed, as a measure of effectiveness and this paper attempts to fill that gap in the previous research.

This work relies heavily on various simulation models for experimenting with signal timings under controlled conditions and for estimation of emissions and dispersion of pollutants. The simulation models used are all well known models that have been repeatedly used, validated and documented. VISSIM is used for traffic simulations for generating vehicle performance data, CMEM is used for generating vehicle emissions and CAL3QHC for CO dispersion.

2 METHODOLOGY

Vehicle flow data was collected in 15 min. increments for the morning peak hour in October, 2005 at a busy traffic intersection (Baker Street and Marylebone Road) in London. The layout of the intersection is shown in Figure 1. Simulations were carried out for a comprehensive range of wind speed and headings. Data was also collected on traffic composition by mode, signal timings, intersection geometry, queue discharge rate and crossing pedestrian flows. The intersection was coded in VISSIM micro-simulation software as an isolated traffic intersection. The signal timings were changed in increments of 10 sec. The signal changes consisted of changing the times available to traffic on the Marylebone Road (except for right turning traffic in the eastbound direction). Timings for Baker Street were constant for all signal cycles. The traffic flow was also kept constant.

* *Corresponding author:* Robert B. Noland, Centre for Transport Studies, Department of Civil and Environmental Engineering, Imperial College London, UK. Email: r.noland@ic.ac.uk

The coded model was calibrated to result in the same mean queue discharge rate as was observed in the field. An initial simulation run was carried out with a signal cycle length of 96 sec. as was observed during high flow rates on site. Based on changes in vehicle velocity and acceleration, the journey distance was divided into five zones.

Pedestrian crossings were stretched to 4 m beyond the curb to include pedestrian waiting time in the road crossing travel time. Pedestrians were coded with default VISSIM pedestrian parameters as no-interaction type; where pedestrian movements are not influenced by the presence of other pedestrians. The pedestrian speed range was coded as 50 to 100 percentile speed for adult pedestrians on road crossings as given by Sjostedt (1967) to give a minimum speed of 1.4 m/s which corresponded to the pedestrian behaviour observed in the morning peak hour. Pedestrian compliance to traffic signals was also coded in line with field observations and the simulated pedestrian phase was extended to 1 sec. before and half the clearance interval after the actual pedestrian green phase on all pedestrian crossings.

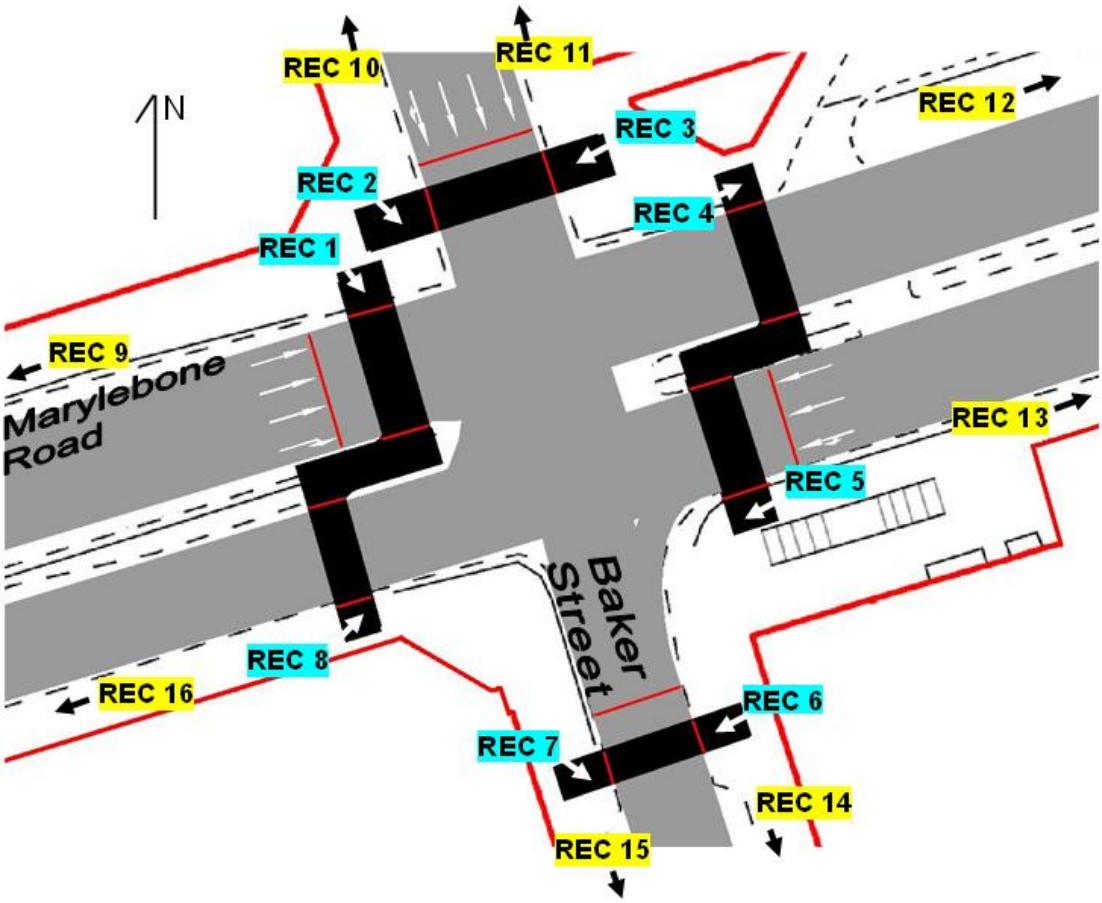

Figure 1. Layout of the Marylebone Road and the Baker Street intersection with the location of stop lines and pedestrian crossings. Receptor locations, as defined in CAL3QHC, are marked with arrows for receptors REC 1 to REC 8. For receptors REC 9 to REC 16 the arrows indicate the direction in which the labelled receptor is located, 60 m further away from their neighbour near-junction receptor.

3 ANALYSIS

All simulations were carried out for a duration of one hour at the maximum possible simulation resolution of 10 simulation-seconds per second. That means 10 data points were generated for every second of simulation run. The high simulation resolution eliminated unexpected acceleration/deceleration surges that may result with low resolution simulations. Vehicle performance data was generated for vehicle speed, acceleration and distance travelled. For pedestrians, data was generated on pedestrian travel times to cross the road. The pedestrian path consisted of actual pedestrian crossings across the vehicle carriageway, the staggered median refuges (on the Marylebone Road) and a 4 m stretch on the curb on either end of the crossing. Pedestrian travel paths were divided into two halves and travel time was recorded separately for each half. Exposure to CO at a

particular crossing x travelling from point a to point b was then expressed by the CO Exposure Index CEI which was calculated as follows

$$CEI_{x(a-b)} = \tau_{1x}\varsigma_a + \tau_{2x}\varsigma_b$$

where τ_{1x} = the travel time on the first half of the crossing x (sec); ς_a = the CO concentration measured at the nearest receptor to a (ppm: parts per million); τ_{2x} = the travel time on the second half of the crossing x (sec); and ς_b = the CO concentration measured at the nearest receptor to b (ppm). The CMEM output was used to generate emissions for CO for each of the 15 datasets. CAL3QHC requires two separate emission values for each link defined in it (15 links in our case). The first value is based on emissions from all the vehicles for their whole journey (per unit distance) while the second value is based on emissions only for the idling state of the vehicles (per unit time). Emissions for idling vehicles were obtained when the vehicle speeds were zero. These emission values obtained from the CMEM were then used as input to the CAL3CQH pollutant dispersion model along with data on signal timings, network coordinates, receptor locations, meteorological data and traffic data. Traffic and signal timings data was obtained from the VISSIM simulations while for the meteorological data wind speeds from 1 m/s to 20 m/s and headings from 1 to 360 degrees (1 degree increments) were employed.

Background concentrations in CAL3QHC were assumed to be zero. Sixteen receptors were coded as shown in Figure 1. These are receptors 1 to 8 (REC 1 to REC 8 in Figure 1) at 3 m from the curb at each end of the pedestrian crossing, and receptors 9 to 16 (REC 9 to REC 16) at a distance of 60 m (away from the intersection) and from the receptors at the pedestrian crossing ends. No receptor was placed on the pedestrian crossings across the carriageway or on the pedestrian refuge in the staggered pedestrian crossings. This was because CAL3QHC defines a mixing zone for pollutants (CO in this case) that extends to 3 m on either side of the vehicle carriageway.

4 RESULTS

Carbon monoxide concentrations were estimated at the receptors for a one hour simulation period. The worst case scenarios in terms of wind speed and headings are discussed. Wind speed of 1 m/s invariably resulted in the maximum observed concentrations while different receptors experienced maximum concentrations at different wind headings. For each receptor the highest concentration out of all 360 results for the wind headings is used. Results show that CO concentration drops rapidly with increasing wind speed until about 4 m/s after which the change is more gradual.

Analyzing results for changes in wind headings along the Marylebone Road it is observed that higher concentrations take place when wind is blowing somewhat parallel to the road along which the receptor is located, although the peaks do not occur at exact parallel headings. Low concentrations result when winds are blowing perpendicular to the road direction. However for receptors along Baker Street, these results hold only for receptors REC 11 and REC 14 which are located away from the intersection. Receptors near the pedestrian crossings on the intersection show a more complex variation as a large proportion of emissions actually come from traffic on the Marylebone Road.

The change in CO concentration at various receptors with changes in signal cycle length is illustrated by the bar charts in Figure 2 for a soak time of zero (i.e., optimal emissions control performance). The results from each receptor can be broadly separated into three categories.

- CO concentrations decrease with increasing signal cycle length along Marylebone Road. Representative results from this group are shown for receptors REC 1 and REC 5 which are located near pedestrian crossings in front of stop lines for approaching traffic from either direction of the Marylebone Road. Other receptors located along the Marylebone Road display similar trends, though the magnitude of CO concentrations is smaller on the discharge roads in comparison to the approach roads. These results reflect the increased green time available to traffic on the Marylebone Road with increasing signal cycle resulting in less idling and subsequent accelerating vehicles. However there is a draw back and that is pedestrians have to wait longer on the curbside. Hence, even if the emissions decrease per unit time pedestrian exposures increase especially as pedestrians cross north to south (see Figure 3).

- CO concentrations decrease with increasing signal cycle length on Baker Street approaches. Results representative of this group are shown for receptors REC 2 and REC 3 both of which are located near the pedestrian crossings in front of stop lines for the approaching Baker Street traffic. As the signal cycle increases the green time available to traffic on the Baker Street remains constant which results in an increase in idling vehicles waiting for longer times on the stop line. The receptors would have recorded increasing CO concentrations with an increase in signal cycle lengths if only emissions from Baker Street were considered in isolation. These receptors are, however, also exposed to emissions from the nearby eastbound Marylebone Road which not only offsets any expected increase but, shows a decrease in emissions with increasing signal cycle durations. Receptors on the discharge arm of Baker Street also show similar results but in their case the results are due to comparatively lower traffic flow and large available green times for the vehicular traffic.
- An increase in CO concentrations with increases in signal cycle length. Two receptors show this trend; REC 10 and REC 11. These receptors are located away from the intersection on the approach arm of the Baker Street and are somewhat immune to the emissions generated by traffic at the Marylebone Road hence they are able to pick up the increased emissions resulting from increasing traffic queues forming on Baker Street as the green time available for cross traffic falls, in parallel with reduced pedestrian green time.

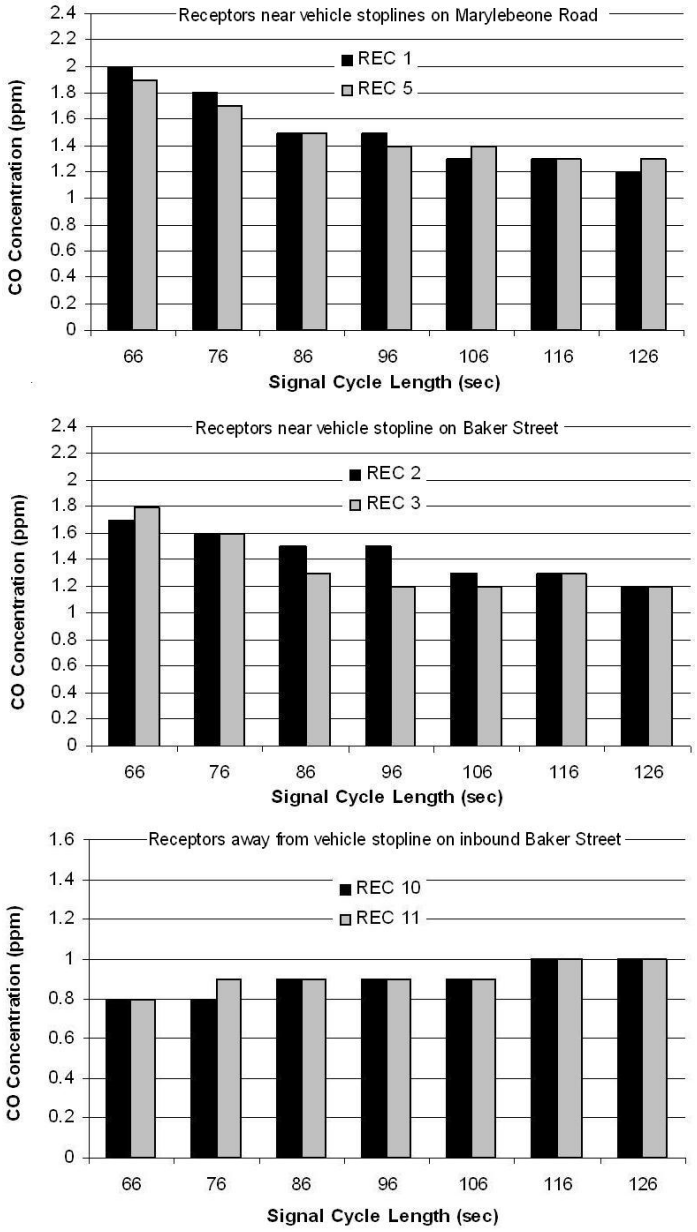

Figure 2. Change in CO concentrations with change in signal cycle length for 1 m/s of wind speed and worst case scenario for wind direction.

In terms of magnitudes the receptors nearer the intersection record higher concentrations than those further away. This difference is, however, small when the more distant receptors are located on the approach arm of the road on which traffic is queuing.

Pedestrian exposure is shown graphically in Figure 3 based on the CO Exposure Index defined above. Pedestrians crossing the Marylebone Road north to south face the largest levels of exposure to CO in magnitude and face the largest increase with increasing signal cycle lengths. This is because they have the shortest pedestrian green phase of all the pedestrian crossings in the intersection and must cross the path of the heaviest traffic flow. While waiting on the curbside pedestrians on these crossings are also exposed to the idling traffic on the inbound Baker Street further increasing their exposure levels. For pedestrians crossing the Marylebone Road from south to north the exposure is less mainly because they have to stay on the staggered pedestrian refuge for a shorter duration compared to those crossing from north to south. This is due to the sequence of changes in signal phases which provide better coordination for pedestrians crossing from south to north.

Pedestrians crossing the Baker Street inbound arm benefit from increased signal cycle lengths as the length of the pedestrian phase also increases correspondingly. For the pedestrians crossing on the outbound arm of Baker Street the pedestrian phase remains constant and hence the available time for pedestrians to cross the road decreases in real terms as the signal cycle increases.

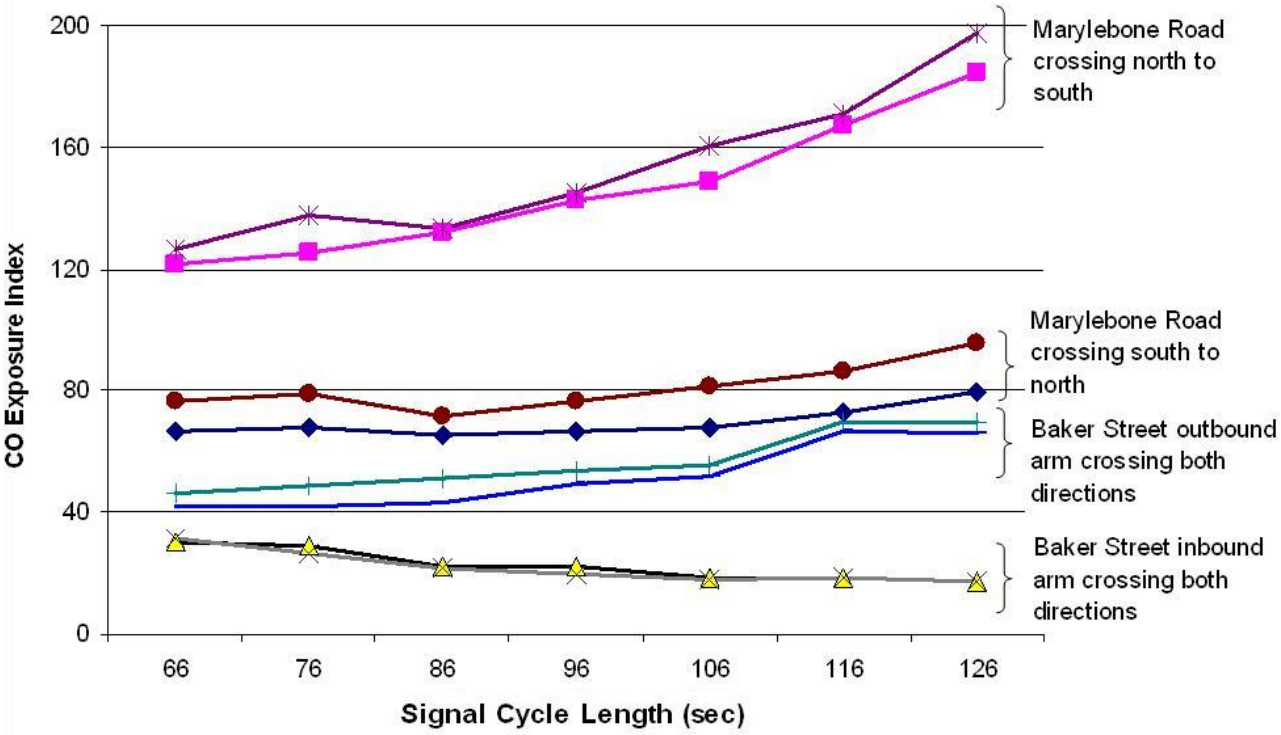

Figure 3. Pedestrian CO exposure for the four pedestrian crossings (both directions). CO Exposure Index is the multiplicative factor of mean pedestrian crossing time (including waiting time at the curb) and the CO concentrations recorded at the nearest receptors.

5 CONCLUSIONS

This work has illustrated how changes in signal cycle timings result in changes in pollutant exposure of pedestrians at pedestrian crossings. There is clearly a trade-off between pedestrian exposure and the reduction in emissions as a result of smooth traffic flow, achieved usually by employing longer signal cycle lengths. Long signal cycles, resulting in less total vehicle emissions, cause increased pedestrian delay and longer exposure to slightly reduced emission levels. Measuring this trade-off would require devising values of time for pedestrians in terms of exposure to harmful pollutants such as CO in addition to delays in terms of lost time. No such work is currently available and this is clearly an area open for further research.

This work has also highlighted a number of intersection traffic control measures that allow smooth traffic flows and reduce vehicle delays but increase pedestrian exposure to vehicle emissions. The

first is the use of long signal cycle times which has already been discussed. The second is the use of a parallel pedestrian phase where pedestrians cross the road only when the vehicular traffic on the parallel road is also moving. This technique further allows for dividing a single road crossing into two multiple arms and pedestrians have to wait twice to cross a single road; once at the curb and again at the refuge while also increasing their geometric delay through staggering of the median refuge and hence further increasing their exposure. As shown in the results the pedestrians who cross the staggered crossing with some measure of coordination between the two legs are less exposed to pollutants than those who have to spend greater time on the refuge.

REFERENCES

Ishaque, M.M. and R.B. Noland, 2005a: A multimodal micro-simulation of vehicle and pedestrian signal timings. *Journal of the Transportation Research Board: Transportation Research Record*. 1919, 107–114.

Ishaque, M.M. and R.B. Noland, 2005b: Trade-offs between vehicular and pedestrian traffic using micro-simulation methods. Paper presented at the *16th International Symposium on Transport and Traffic Theory (ISTTT)*, College Park, Maryland.

Sjostedt, L., 1967: Behaviour of pedestrians at pedestrian crossings. National Swedish Road Research Institute. Quoted by R.B. Sleight, 1972 in The Pedestrian. Ed. T.W. Forbes' *Human factors in traffic safety research*.

ACKNOWLEDGEMENT

We acknowledge support from the Rees Jeffreys Road Foundation for which we are grateful.

Potential methods to include the full climate impact of aviation emissions into the European Emissions Trading Scheme and their scientific integrity

D. S. Lee*
Dalton Research Institute, Manchester Metropolitan University, John Dalton Building, Chester Street, Manchester M1 5GD, United Kingdom

R. C. N. Wit
Natuur en Milieu (N&M) Donkerstraat 17 Utrecht, Postbus 1578, 3500 BN, the Netherlands Utrecht NL

Keywords: Aviation emissions, emissions trading scheme, metrics.

ABSTRACT: The European Commission has expressed a preference that for future inclusion of aviation into the European Emissions Trading Scheme, non-CO_2 effects should be accounted for. Three scenarios are outlined here: utilizing some 'multiplier' on CO_2 emissions; accounting for non-CO_2 effects on a flight-by-flight using an approach that would be compatible with GWPs; and utilizing alternative policy instruments for the non-CO_2 effects. All approaches had serious difficulties in terms of their scientific integrity. A multiplier approach using radiative forcing, or its direct derivatives was shown not to be robust. There are difficulties with formulating GWPs for ozone and contrails. Other policy instruments such as a NO_x landing charge and cruise NO_x charges were considered: NO_x landing charges may not be a good proxy for cruise NO_x, whereas NO_x en-route charges were technically robust, relatively straightforward but have difficulties with their political acceptability.

6 INTRODUCTION

Aviation contributes to climate change through its carbon dioxide (CO_2) and other emissions/effects (IPCC, 1999). In 2002, international civil aviation accounted for 2.8% of the total national CO_2 emissions across the 25 Member States of the European Union and increased by 60% over the last decade. This increase is a result of demand for air transport which has outpaced improvements in fuel efficiency arising from engine/aircraft technology and in the air traffic control system. Thus, without any policy intervention, the growth of global CO_2 emissions from aviation is expected to double in the coming decades.

In addition to emissions of CO_2, aviation contributes to climate change through emissions of nitrogen oxides (NO_x), which are particularly effective in forming the greenhouse gas ozone (O_3) when emitted at subsonic aircraft cruise altitudes. Aircraft also trigger the formation of contrails in certain conditions and may enhance the formation of cirrus clouds, both of which add to the overall global warming effect. In 1999 the Intergovernmental Panel on Climate Change (IPCC) estimated that the total radiative forcing (RF) from aviation was 2.7 times that of its CO_2 RF alone in 1992 (this ratio was termed the Radiative Forcing Index, or RFI), excluding potential cirrus cloud enhancement. More recent data on aviation's radiative impact for 2000 (Sausen et al., 2005) imply an RFI of 1.9, once again excluding cirrus cloud enhancement. This means the environmental effectiveness of any mitigation policy will depend on the extent to which these non-CO_2 effects are also taken into account and the time-frame over which 'effects' are considered and quantified.

The European Commission has stated a preference for the inclusion of all aviation's climate impacts into the European Emissions Trading Scheme (E-ETS). In this work, three potential scenarios by which this might be achieved were examined where the scientific/technical integrity was a pre-

* *Corresponding author:* D. S. Lee, Dalton Research Institute-CATE, Manchester Metropolitan University, Faculty of Science and Engineering, John Dalton East Building, Chester St, Manchester M1 5GD, UK. Email: D.S.Lee@mmu.ac.uk

requisite. They are: firstly, by utilizing a 'multiplier'; secondly, by considering an individual 'effects-based' approach; and lastly a CO_2 approach with so-called 'flanking instruments' (i.e. additional policies or measures) to cover non-CO_2 effects (Wit et al., 2005). This work and its other economic and policy impacts are documented in greater detail elsewhere (Wit et al., 2005).

7 THE 'MULTIPLIER' APPROACH

In this approach, CO_2 is traded but some multiplier is used to capture the non-CO_2 effects. The IPCC (1999) introduced the radiative forcing index (RFI) as a means of comparing the total radiative effects from aviation to its CO_2 RF over some emissions scenario. Usage of the RFI as a multiplier for *emissions* is unsuitable as it does not take into account future effects of CO_2 in the way that the Global Warming Potential (GWP) does since RF is essentially a *backward looking* metric (since it includes CO_2's history). Moreover, the value of the RFI is not a constant and is entirely dependent upon the emissions scenario adopted – the close agreement found the between 'present day' value of 2.7 and 2.6 for 2050 for scenario Fa1 by the IPCC (1999) was entirely fortuitous. This was demonstrated by Wit *et al*. (2005). If a hypothetical scenario is conceived whereby emissions remain constant after 2000, it can be seen that RFI damps and CO_2 forcing increases over time (see Fig. 1).

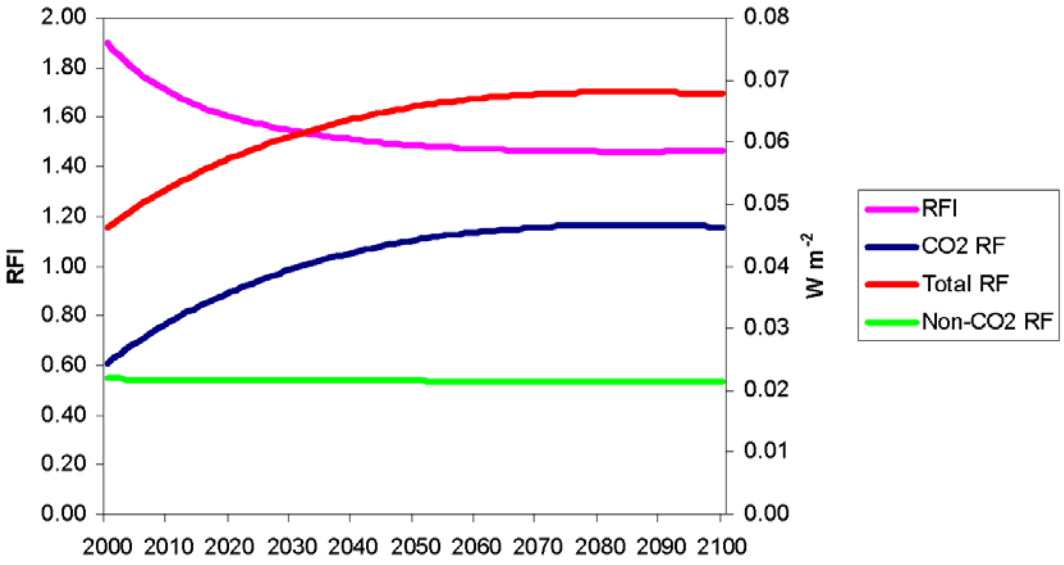

Figure 1. Modelled RFI and RF for aviation using constant 2000 emissions, model tuned to Sausen et al. (2005) forcings.

The Global Temperature Potential (GTP) (Shine et al., 2005) has been shown to be close to GWP in that it allows a comparison of a global mean temperature response from some forcing to that from CO_2 over some arbitrary time horizon. If an RFI is reformulated using GTPs for constant emissions (Global Temperature Index – GTI), a linear relationship between CO_2 *emissions* and CO_2 and non-CO_2 temperature effects is apparent (note that this calculation assumes efficacies of non-CO_2 forcings of unity). Such an approach is attractive in that it more closely relates the total effect to the *emissions* of CO_2 but in progressing further down the cause-effect chain, it introduces more complexities and therefore uncertainties. Over a 100 year time-integration for *constant* emissions, non-CO_2 effects comprise approximately 30% of the total temperature effect and CO_2 represents 70%: this attribution is clearly different if an actual emission scenario is considered. Currently, the underlying GTP has only been used for constant emissions *c.f.* a pulse, as in the GWP. A pulse response is perhaps more useful in terms of determining a response to a marginal emissions change. More work is needed to test whether the GTP and derivative GTI can be used to determine an emissions multiplier for aviation CO_2 to capture non-CO_2 effects but the initial results are promising.

Thus, it is concluded that RFI cannot be used with scientific integrity as a multiplier but a GTI may be useful but requires more work.

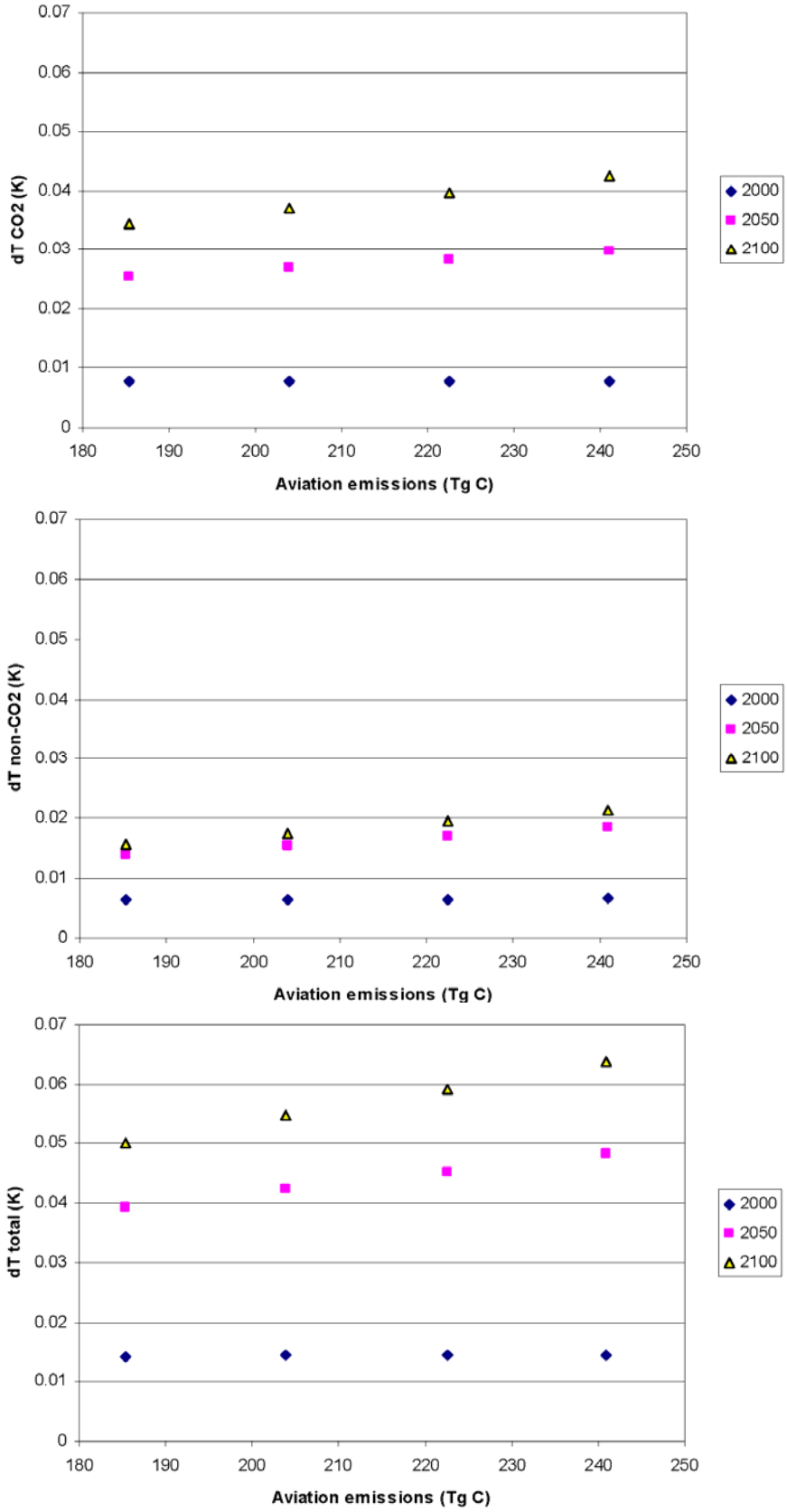

Figure 2. Modelled temperature response for CO_2 (a), non-CO_2 (b) and total (c) aviation effects for constant CO_2 emissions at 2000, 2050 and 2100 for different emission rates.

8 'EFFECTS-BASED' APPROACH

The aim of this approach was to examine whether individual non-CO_2 effects of aviation could be addressed using *different metrics* that might be compatible with the GWP under an emissions trading scheme. This approach requires a consideration of effects on an individual flight basis.

A flight-based approach for non-CO_2 effects requires sophisticated modelling to account for O_3/CH_4 changes from NO_x emissions, and contrails/cirrus. Such models are still in the research domain and it is not possible to recommend one over another. Moreover, the aircraft impact depends upon the background conditions and these conditions – and the ultimate effect – are time and space dependent. If it were possible to agree a model and it was accepted that globally, aggregated emissions produce a certain global production rate of O_3, then under such assumptions it might be reasonable to disaggregate an O_3 (mass) production rate per unit mass NO_x. However, to take such disaggregation to the next level, i.e. RF, and disaggregate to individual flights, involves more assumptions that are difficult to justify at such a level of detail.

For contrails, similar difficulties arise: there are uncertainties in the calculation of both contrail coverage and the RF. Again, to attribute an effect down to an individual flight level cannot currently be done robustly since environmental conditions dictate whether a contrail is formed or not and the RF effect depends *inter alia* on time of day.

For calculating both O_3 and contrail effects on a flight-by-flight basis, this would only be possible on a statistical basis or by accepting an approach of scaling a global estimation of the effects to a flight km basis assuming a linear relationship.

It is, in principle, possible to formulate a GWP for O_3 but this is a contentious issue, vigorously debated in the literature; for contrails, it is not possible to derive a GWP since a contrail cannot be easily related to a mass emission. Therefore, this approach cannot be recommended.

9 FLANKING INSTRUMENTS

In this approach, CO_2 is covered by the E-ETS and 'flanking instruments' would be used to tackle non-CO_2 effects – i.e. by using more than one policy instrument. A critical question with a CO_2-only scheme is whether any *negative* tradeoffs will occur as a result. Historically, the overall emissions index of the fleet for NO_x ($EINO_x$ – g NO_x/kg fuel) has increased as a result of higher combustor temperatures and pressures that have resulted from increases in the fuel efficiency of gas turbine engines. But, under this approach, the question is whether the $EINO_x$ increase would proceed at a *faster* rate if aviation were incorporated into the E-ETS because of an increased impetus to reduced CO_2? Engine manufacturers claim that this would not be the case but this remains uncertain with increasing fuel prices. In addition, modern engines have a higher propensity to cause contrails over a greater depth of the atmosphere than was the case with older technology (Schumann et al., 2000). This is expected to increase in the future, based upon assumptions over the increase in propulsive efficiency (η). It has been suggested that values of η for 2050 will result in 20% greater contrail coverage over today's global estimation of η (Gierens et al., 1999). Thus, it is concluded that negative tradeoffs are more likely than not to occur under the scenario of aviation being incorporated into a CO_2-only emissions trading scheme, without flanking instruments. However, for contrails and contrail-cirrus, the magnitude of the RF effect is still rather uncertain.

The current ICAO landing/take-off cycle (LTO) NO_x Certification regime provides one potential flanking instrument. The $EINO_x$ over the LTO cycle has been claimed by industry and an ICAO Working Group to correlate with cruise $EINO_x$ although no formal statistical correlation has been presented. The disadvantage to this approach is that Certification limits engine NO_x (amongst other things), according to overall pressure ratio of the engine. Since the $EINO_x$ has increased as a result of moving to higher overall pressure ratios, this approach would leave open the possibility of NO_x actually *increasing* if the $EINO_x$ increased at a rate greater than fuel consumption decreased.

Alternatively, an airport NO_x landing charge might be employed. If a landing charge were introduced, this could be done independently of ICAO and if implemented on a mass NO_x/landing charge (using ICAO NO_x Certification data), this would bring pressure to utilize lower-NO_x technologies that would have a co-benefit for local air quality. This approach, whilst crude, and only

tackling NO_x, is critically dependent upon the claim of a 'correlation' between LTO $EINO_x$ and cruise $EINO_x$.

Perhaps the most effective flanking instrument that has the fewest uncertainties would be to formulate a cruise NO_x charge. Emissions of NO_x can be calculated within an uncertainty of ±10% from fuel consumption (which is known accurately and could be reported by the airline on a flight-by-flight basis) and the industry could calculate this with much more accuracy from engine performance models. Unfortunately, the concept of emissions *charges* has proved to be very contentious, particularly within the ICAO forum and the potential political acceptability is low.

10 CONCLUSIONS

Formulating a scientifically robust metric for dealing with non-CO_2 effects of aviation on climate that can be incorporated into an emission trading regime is represents a challenge.

Multiplying CO_2 emissions by an RFI is inherently unsuitable although a temperature-based metric under development over an integration time-period (similar to a GWP) appears promising.

No suitable metrics have been found for non-CO_2 effects that can be applied on a flight-by-flight basis that are readily compatible with a GWP.

11 REFERENCES

Gierens K., Sausen R. and Schumann U., 1999: A diagnostic study of the global distribution of contrails part II: future air traffic scenarios. *Theoretical and Applied Climatology* **63**, 1–9.

IPCC 1999: Special report on aviation and the global atmosphere, J.E. Penner, D.H. Lister, D.J. Griggs, D.J. Dokken, M. McFarland (Eds), Cambridge University Press, Cambridge, UK.

IPCC 2001: Climate change 2001: The scientific basis. Contribution of Working Group 1 to the Third Assessment Report, J.T. Houghton (Eds), Cambridge University Press, Cambridge, UK.

Lim L. L., D. S. Lee, R. Sausen, and M. Ponater 2007: Quantifying the effects of aviation on radiative forcing and temperature with a climate response model. Manuscript to be submitted.

Sausen R. and U. Schumann, 2000: Estimates of the climate response to aircraft CO_2 and NO_x emissions scenarios. *Climatic Change* 44, 27-58.

Sausen R., I. Isaksen, V. Grewe, D. Hauglustaine, D. S. Lee, G. Myhre, M. O. Köhler, G. Pitari, U. Schumann, F. Stordal, and C. Zerefos, 2005: Aviation radiative forcing in 2000: and update on IPCC (1999). *Meteorologische Zeitschrift* **114**, 555–561.

Schumann, U., R. Busen, and M. Plohr, 2000: Experimental test of the influence of propulsion efficiency on contrail formation, *Journal of Aircraft, **37***, 1083–1087.

Sausen R., Isaksen I., Grewe V., Hauglustaine D., Lee D. S., Myhre G., Köhler M. O., Pitari G., Schumann U., Stordal F. and Zerefos C. (2005) Aviation radiative forcing in 2000: and update on IPCC (1999). *Meteorologische Zeitschrift* **114**, 555 – 561.

Shine K. P., Fuglestvedt J. S., Hailemariam K., Stuber N. (2005) Alternatives to the global warming potential for comparing climate impacts of emissions of greenhouse gases. *Climatic Change* doi:10.1007/s10584-005-1146-9.

Wit R. C. N., Boon B. H., van Velzen A., Cames M., Deuber O. and Lee D. S. 2005: Giving wings to emission trading. Inclusion of aviation under the European emission trading system (ETS): design and impacts. CE-Delft, No. ENC.C.2/ETU/2004/0074r, the Netherlands.